10/21/91 JM

10-7-91

SANDIA REPORT

SAND88—0810 • UC—814
Unlimited Release
Printed September 1991

Yucca Mountain Site Characterization Project

Preliminary Numerical Modeling for the G-Tunnel Welded Tuff Mining Experiment

Roy L. Johnson, Stephen J. Bauer

Prepared by
Sandia National Laboratories
Albuquerque, New Mexico 87185 and Livermore, California 94550
for the United States Department of Energy
under Contract DE-AC04-76DP00789

"Prepared by Yucca Mountain Site Characterization Project (YMSCP) participants as part of the Civilian Radioactive Waste Management Program (CRWM). The YMSCP is managed by the Yucca Mountain Project Office of the U.S. Department of Energy, DOE Field Office, Nevada (DOE/NV). YMSCP work is sponsored by the Office of Geologic Repositories (OGR) of the DOE Office of Civilian Radioactive Waste Management (OCRWM)."

Issued by Sandia National Laboratories, operated for the United States Department of Energy by Sandia Corporation.

Available to DOE and DOE contractors from
Office of Scientific and Technical Information
PO Box 62
Oak Ridge, TN 37831

Prices available from (615) 576-8401, FTS 626-8401

Available to the public from
National Technical Information Service
US Department of Commerce
5285 Port Royal Rd
Springfield, VA 22161

NTIS price codes
Printed copy: A04
Microfiche copy: A01

SAND--88-0810

DE92 000944

SAND88-0810
Unlimited Release
Printed September 1991

PRELIMINARY NUMERICAL MODELING FOR THE G-TUNNEL WELDED TUFF MINING EXPERIMENT

Roy L. Johnson
Engineering and Structural Mechanics Division

Stephen J. Bauer
Geotechnical Design Division

Sandia National Laboratories
Albuquerque, NM 87185

ABSTRACT

Yucca Mountain, located in Southern Nevada, is to be considered as a potential site for a nuclear waste repository. Located in Rainier Mesa on the Nevada Test Site, G-Tunnel has been the site of a series of experiments, part of whose purpose is to evaluate measurement techniques for rock mechanics before testing in the Exploratory Shaft. Rainier Mesa is composed of welded and nonwelded tuffs that have thermal and mechanical properties and stress states similar to those of tuffs expected to be encountered at Yucca Mountain. A series of finite element calculations were performed to aid in designing instrumentation for the experiments in G-Tunnel and later to correlate with measured data.

In this report are presented the results of the preliminary finite element calculations performed in conjunction with experimental measurements of drift convergence, or closure, and rock mass relaxation zones made before, during, and after completing the welded tuff mining experiment in G-Tunnel. Tape extensometer measurements of drift convergences and measurements determined by multiple point borehole extensometers are compared with corresponding calculated values using linear elastic and jointed rock material models.

The calculations performed as part of this report were done in support of evaluating this type of prototype test. They were used initially to assist in experiment design. Later analyses, and those planned for the future, are to be directed towards better understanding the physical phenomena associated with developing excavations in welded tuff. These analyses are not intended for direct use in licensing. Further, these analyses were very preliminary in nature.

The quality assurance of the analyses was maintained through a combination of the iterative nature of the work and the technical, management, and policy reviews to which the work was subjected.

CONTENTS

FIGURES

FIGURES (Cont.)

TABLES

1.0 INTRODUCTION

1.1 Background

Yucca Mountain, located in southern Nevada, is to be characterized as a site for a potential nuclear waste repository. A series of rock mechanics experiments have been conducted in G-Tunnel, located in Rainier Mesa on the Nevada Test Site (NTS). One purpose of the experiments is to evaluate measurement techniques for rock mechanics before testing in the Exploratory Shaft. Rainier Mesa is composed of welded and nonwelded tuffs that have thermal and mechanical properties and stress states similar to those of tuffs expected to be encountered at Yucca Mountain. To aid in designing the instrumentation required for the experiments in G-Tunnel, and to later correlate with measured data, a series of finite element calculations were performed.

1.2 Scope of this Report

Presented in this report are preliminary results of finite element calculations performed in conjunction with experimental measurements of drift convergence, or closure, made before, during, and after completion of the mining experiment on welded tuff in G-Tunnel. These calculations were performed for three reasons: (1) to aid in the design of the instrumentation layout, (2) to incorporate information regarding stratigraphy that was encountered during the mining operation, and (3) to compare results from the numerical model with actual measured data. These results are considered preliminary because details of the structural geology, such as faults and fractures, were not included in this series of analyses.

A previous set of analyses (Reference 1) showed that more than half of the deformation around a room, incurred as a result of its excavation as the mining face advances, occurs before displacement gages can be installed at the room face. This understanding has a significant impact on the interpretation of the analyses performed for this report. For the two-dimensional plane-strain analysis performed, a hypothetical, infinitely-long drift, instantaneously excavated is the one actually modeled.

The first set of calculations is reported in a letter memorandum dated June 29, 1984, a copy of which is included as Appendix A. A second set of calculations was performed to incorporate a change in the geometry of the roof of the Demonstration Drift and to refine the finite element mesh in the vicinity of the Demonstration Drift. The first and second sets of calculations are summarized in Section 2.5 of this report. The emphasis in this report is on the third or latest set of calculations, and, unless otherwise noted, all detailed results and discussions are referred to this third set.

A complete description of the geometry and geomechanical measurements initially planned for this experiment is contained in Reference 2, and measurements are summarized in Reference 3. A plan view of the mined drifts, showing measurement stations and principal faults and fractures, is shown in Figure 1(a). Figure 1(b) is a cross section showing locations of measurement lines consisting of multiple point borehole extensometer (MPBX) and borehole deflectometer holes. These locations are referred to when results are presented.

The purpose of the calculated results presented here is to compare computed displacements with measured displacements for this experiment and to provide a basis for calculating predictions of the response of similarly-sized drifts in planned testing in the Exploratory Shaft.

calculating predictions of the response of similarly-sized drifts in planned testing in the Exploratory Shaft.

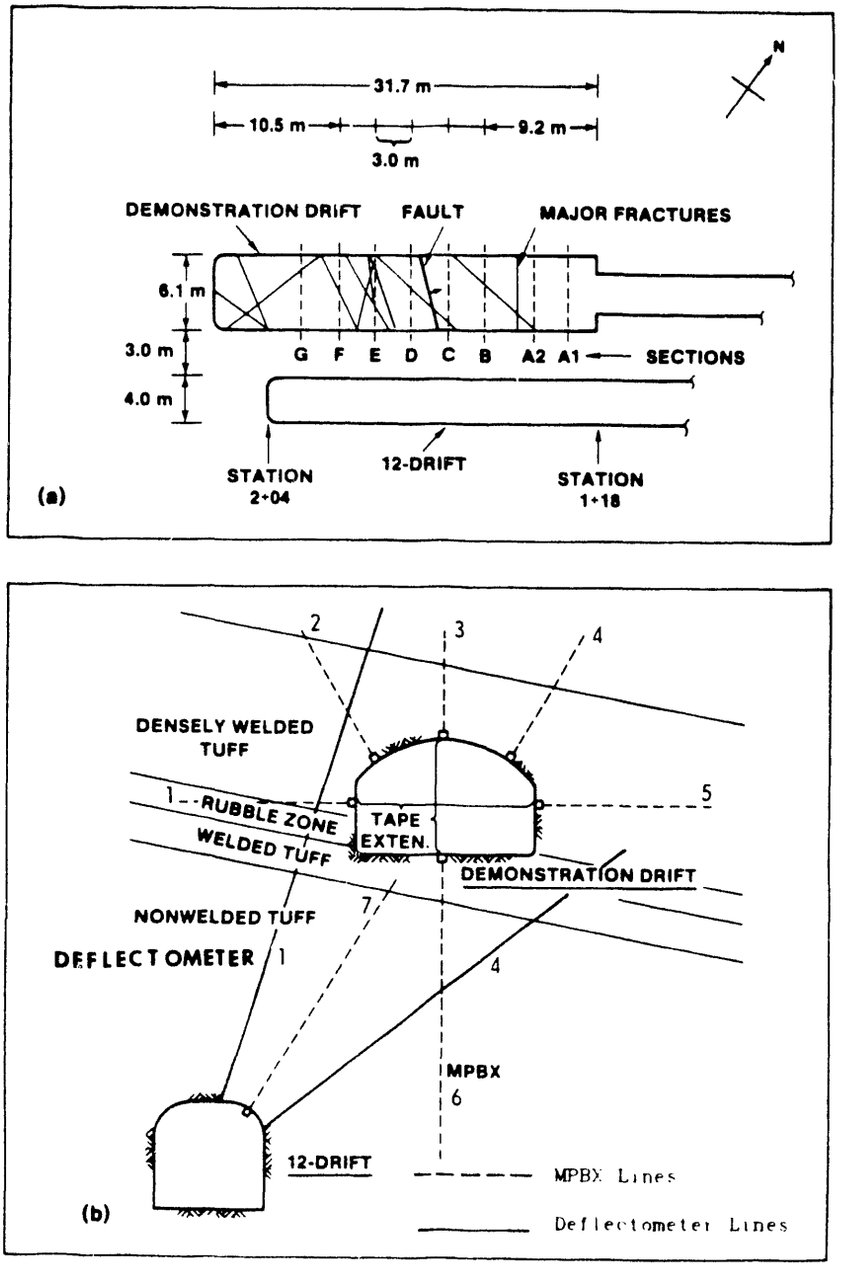

Figure 1. Plan View (a) and Cross Section (b) of the Demonstration Drift [Reference 2]

2.0 FINITE ELEMENT ANALYSES

2.1 Finite Element Model

The two-drift mining experiment was modeled using a plane-strain, linear elastic material model in the computer code JAC (Reference 4). A generic cross section incorporating the major features of the stratigraphy is shown in Figure 2. This stratigraphy is viewed as somewhat representative of conditions at Stations C and E of the Demonstration Drift; however, the stratigraphy lacks any of the geologic structures, such as faults and major fractures that could affect both measurements and analyses. Inclusion of these features would require a three-dimensional model. For this reason the modeling effort requires additional work before it can be considered more than preliminary.

Figure 2 shows the dimensions of the rooms and the size of the region modeled. A mesh consisting of 1,757 four-node, quadrilateral elements and 1,902 nodal points was imposed on this region (Figure 3). In situ stresses with values of -8 MPa vertical and -2 MPa horizontal (a negative sign means compression) were assumed to be constant in all elements of the mesh. Pressure boundary conditions of -8 and -2 MPa, were imposed on the top and the right vertical boundaries, respectively, to equilibrate the in situ stress state. Displacement boundary conditions were zero horizontal displacements along the left vertical boundary and zero vertical displacements along the bottom boundary, corresponding to roller supports along these two boundaries as shown in Figure 2. In a later section, these assumed boundary conditions are compared with another solution where the right vertical boundary is restrained against horizontal motion.

The regions in the vicinity of the drifts were meshed more finely to capture stress and strain gradients and to attempt to suppress any hourglassing that may occur. The phenomenon of hourglassing is discussed below. The boundaries between the finely and coarsely meshed regions were defined as bonded slip lines. Slip lines are normally used to define discrete lines in the mesh along which slip or separation may occur: for example, boundaries between two different materials in contact or a physical separation between two different regions of the mesh exist. In either case, the two regions may move with respect to one another. The slip lines may be used to model major faults or fractures in the material where relative motion of the two surfaces of the discontinuity may occur. In the case of bonded slip lines, no relative displacements are permitted across these boundaries. In the model used in these calculations, slip lines were used to define discontinuities in mesh lines across the boundaries of two regions that were meshed differently but permitted no relative movement of the two regions.

No attempt was made in these calculations to model the complex system of faults and joints encountered along the drifts. It was not possible to do so with a two-dimensional representation because the system of faults and major fractures runs at angles up to 45° with the directions of the drifts introducing anisotropy in the material behavior [Figure 1(a)]. The roof of the Demonstration Drift is placed in the densely welded tuff (Unit B) and the floor, in the basal vitrophyre (Figure 2). These two units are separated by a low-modulus breccia or rubble zone. The dip of the geologic units was taken to be 5° from left to right of the cross section as shown in Figure 2.

The element "death" option in the computer code JAC was used to "kill" or remove elements in the interior of the drifts, and the option was exercised to approximate the actual mining sequence. Elements in the interior of 12-Drift were removed in one calculational step, and then elements in the Demonstration Drift were removed in the next

step. During the first step, the equilibration step, all elements were present. Each calculation step was identified by a kinematic time; however, because the calculations were

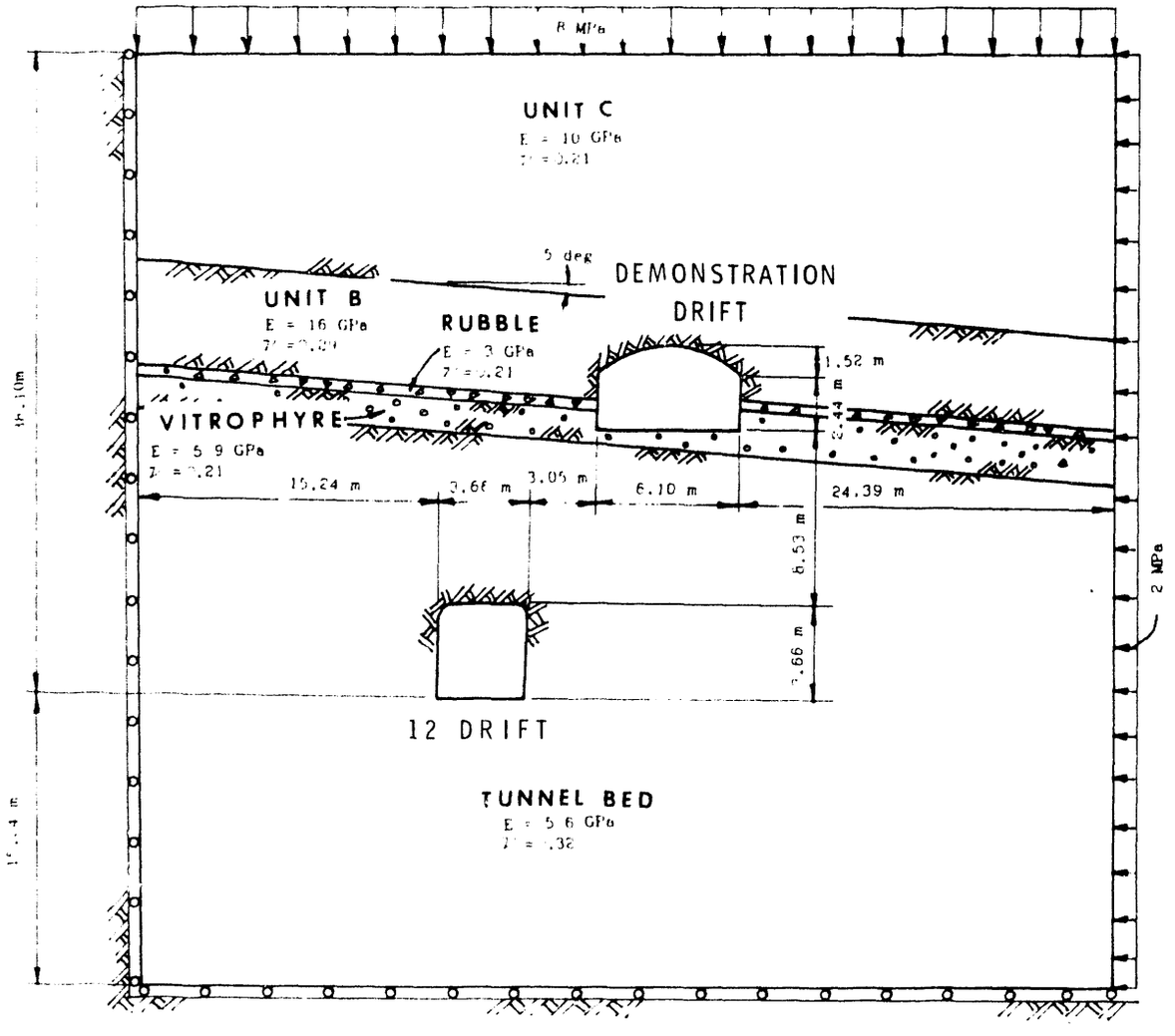

Figure 2. Cross Section of the Meshed Region Showing Principal Stratigraphic Features and Dimensions

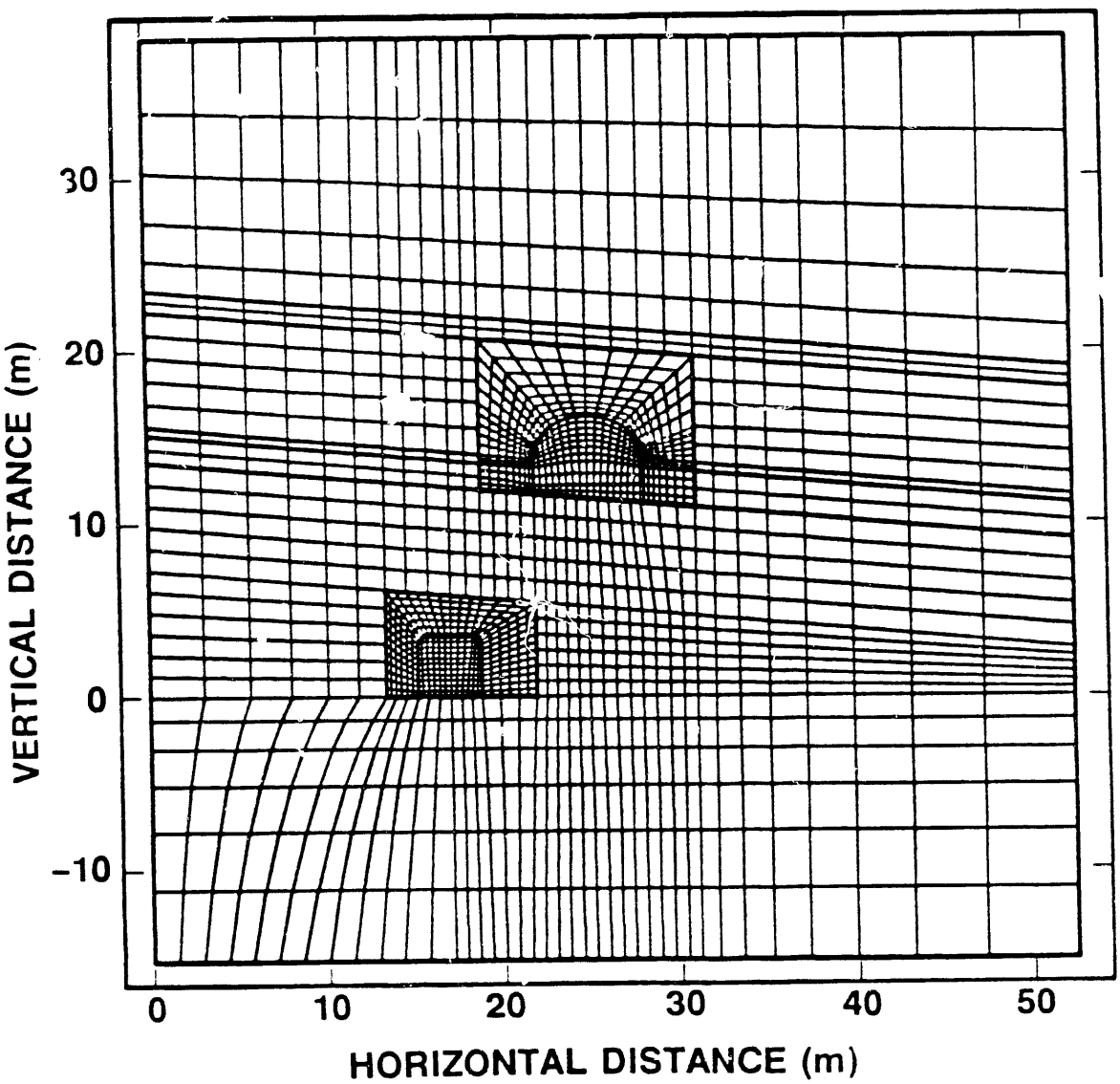

Figure 3. Finite Element Mesh Used in the Calculations

quasi-static, these times served only as an identification. In the plots of results that follow, the times 0, 1, 2, and 3 correspond to the following computational steps:

Time = 0 initialization,
Time = 1 equilibration with in situ stresses,
Time = 2 excavation of the 12-Drift, and
Time = 3 excavation of the Demonstration Drift.

This sequence is illustrated in Figures 4 and 5, which show plots of the deformed mesh at Times 2 and 3.

2.2 Material Properties

Material properties used in these computations are listed in Table 1 by geologic unit. The data were supplied by R. Zimmerman (personal communication), based on his G-Tunnel experience. The values used for unit B (densely welded tuff) are the values listed in Reference 5. No data were available for properties of the rubble, and a value of Young's modulus approximately half that of the vitrophyre was assumed.

2.3 Hourglass Suppression

An instability in the finite element model, hourglassing produces erratic deformation of adjoining elements in an hourglass pattern or keystone shapes of single elements. Hourglassing results from the underintegration of the stiffness matrix of the four-node quadrilateral element and accompanying development of zero-energy modes of deformation. To suppress these spurious modes, an artificial viscosity is introduced in the formulation of the element stiffness matrix (for example, Reference 6).

In the computer code JAC, the default value for artificial viscosity is 1 if no value is specified. In the analyses presented here, the value used ranged from 1 to 100 with intermediate values also considered to assess the effect on the solution. The results presented in this report are those of the latest set of calculations and were obtained with a value of 100 for the artificial viscosity. The effect of hourglass suppression on these results is discussed in Section 3.

2.4 Results of the Computations

Calculated displacements and stresses for locations where experimental data have been obtained are presented here in graph and tabular form. These locations are illustrated in Figure 1(b), where six MPBX positions are shown around the Demonstration Drift. The MPBXs are anchored 15 m into the rock mass and are shown in Figure 1(b) as dashed lines. Two borehole deflectometer holes, No. 1 and 4 [shown as solid lines in Figure 1(b)], extend from the 12-Drift past the Demonstration Drift for distances of 27 and 19.4 m, respectively. In addition, a tape extensometer was used to measure room convergences (inward motion of the roof, the floor, and the room ribs). The nominal locations of the tape extensometer measurement points are also shown in Figure 1(b). Tables 2 and 3 summarize measured and calculated data of drift convergences. The MPBX data listed in Table 3 are limited to the relative movement of one end of an MPBX with respect to the other, over a distance of 15 m. The tape extensometer data in Table 2, however, reflect rock mass movement over a larger region.

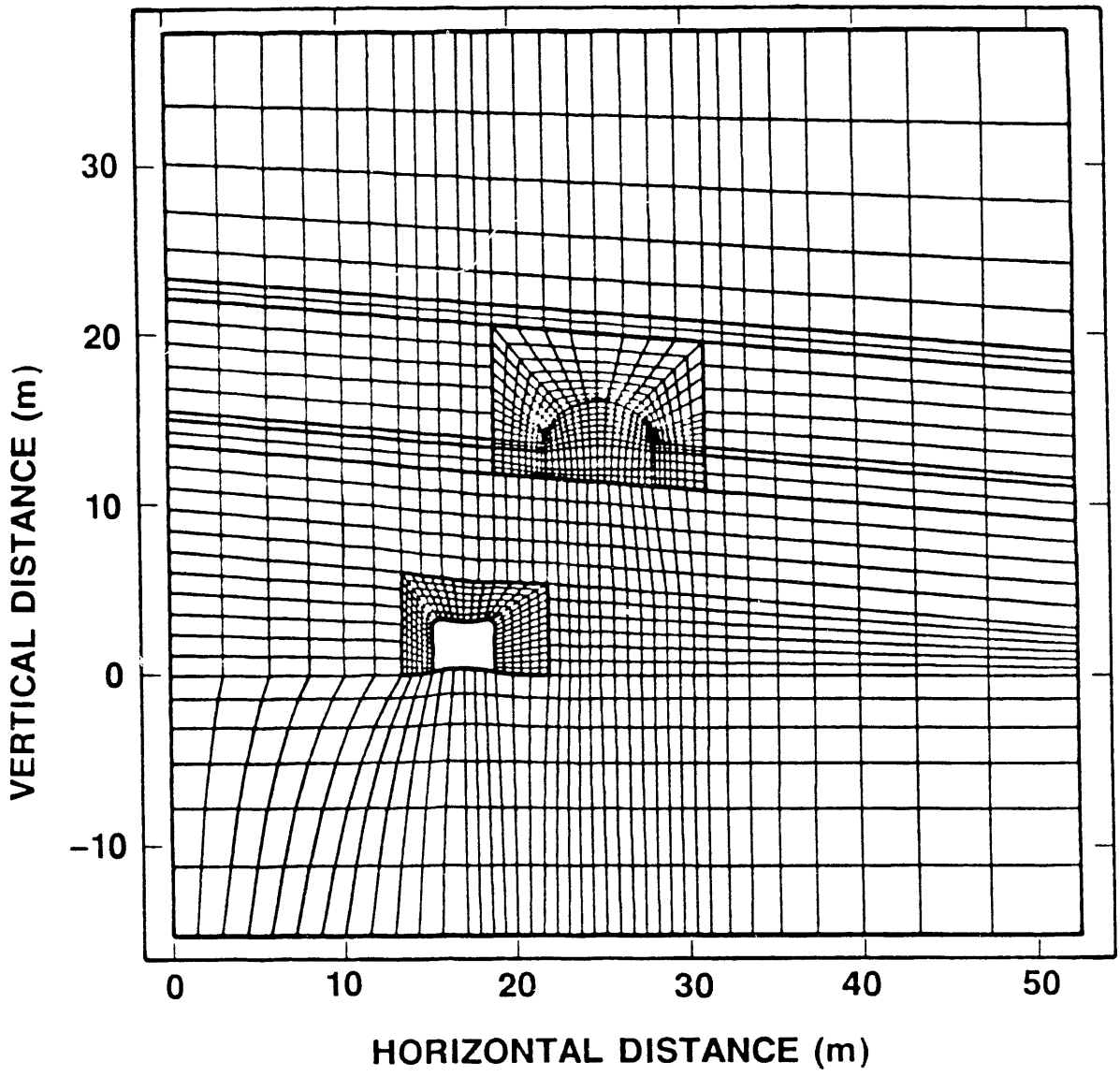

Figure 4. Deformed Mesh After Excavation of the 12-Drift (Time = 2)

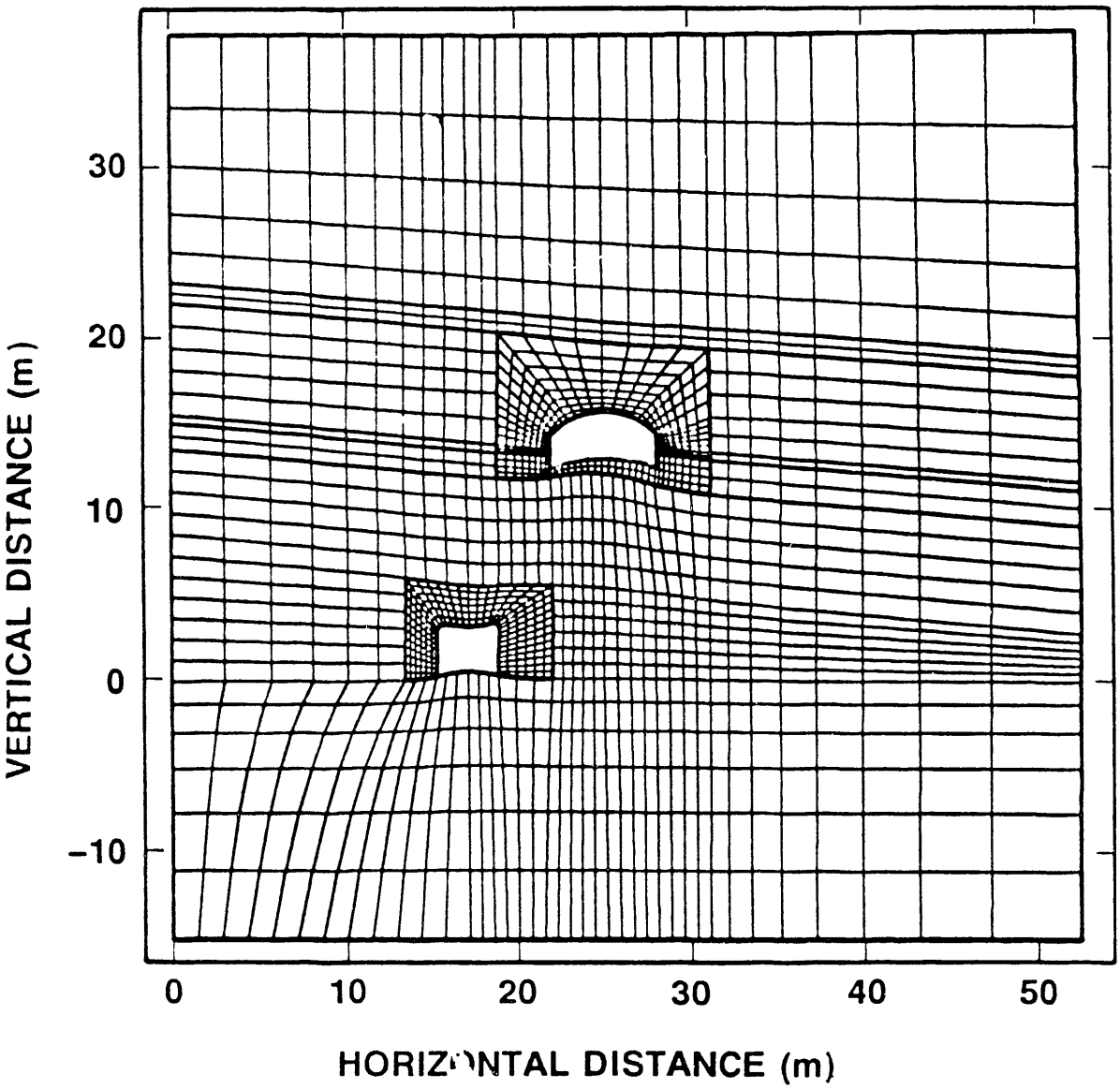

Figure 5. Deformed Mesh After Excavation of the Demonstration Drift (Time = 3)

Unless otherwise noted, all calculated displacements and angle changes are obtained by subtracting the displacements produced by excavation of the 12-Drift (Time = 2) from those obtained after excavation of the Demonstration Drift (Time = 3). The relative displacements so obtained would correspond to experimental measurements in the Demonstration Drift since movement at the rock mass resulting from excavation at the 12-Drift would have occurred before excavation of the Demonstration Drift.

Table 1

Rock Mass Mechanical Properties of Geologic Units

Geologic Unit	Young's Modulus, E (MPa)	Poisson's Ratio, ν
C (moderately welded tuff)	10,000	0.21
B (densely welded tuff)	16,000	0.29
Volcanic Breccia (rubble)	3,000	0.21
Basal Vitrophyre	5,900	0.21
Tunnel Bed Tuff	5,600	0.32

Table 2

Summary of Tape Extensometer Measurements (Reference 3) and Calculated Values of Drift Convergences*

Station	Vertical (mm)	Horizontal (mm)
A2	13.0	-
B	10.8	5.5
C	13.9	10.0
D	17.0	8.2
E	18.5	3.0
F	9.5	2.0
G	9.8	3.0
Average Measured	13.2	5.3
Calculated	12.0	-0.8

* Convergence (inward movement) is positive.

Table 3

Summary of Measured (Reference 3) and Calculated MPBX Convergences*

Station	Vertical			Horizontal		
	Roof (mm)	Floor (mm)	Total (mm)	Left (mm)	Right (mm)	Total (mm)
C	2.5	5.5	8.0	2.4	0.3	2.7
E	2.0	4.0	6.0	-0.5	0.5	0.0
Ave. Meas.	2.3	4.8	7.0	1.0	0.4	1.4
Calculated	2.2	6.6	8.8	0.1	-0.2	-0.1

* Convergence (inward movement) is positive.

2.4.1 Drift Convergences

Figures 6 and 7 are plots of calculated vertical and horizontal displacements along lines coinciding with MPBX Lines 3 and 6 and with Lines 1 and 5, respectively. These lines extend through the Demonstration Drift to the extreme limits of the mesh. These displacements occur after excavation of the Demonstration Drift and indicate the total drift convergences in the vertical and horizontal directions. The vertical convergence is approximately 12 mm and the horizontal divergence less than 1 mm at the rib. Away from the rib, the movement of the rock mass is outward (divergence) with a maximum of approximately 0.6 mm on the left and 0.9 mm on the right. These calculated values compare with measured values of room convergences from tape extensometer measurements of 9.5 to 18.5 mm vertical and 2 to 10 mm horizontal (Table 2 and Reference 3). In addition, some convergence of the drift may have occurred before instrumentation was in place and any measurements were made. Table 2 shows the smallest measured vertical convergence (9.5 mm) occurs at Station F while the largest (18.5 mm) occurs at Station E. The smallest measured horizontal convergence (2 mm) occurs at Station F, and the largest (10 mm), at Station C. At Station E the measured horizontal convergence is approximately 3 mm.

2.4.2 MPBX Displacements

Figures 8 through 14 are plots of calculated and measured displacements along each of the MPBX lines. Displacements along MPBX lines are plotted relative to the end anchor where the displacement is taken as zero. Therefore, the plotted MPBX displacements are changes in length of the MPBX line relative to the anchor. A positive value of displacement indicates an extension of the MPBX, or movement of the rock mass away from the anchor. Measured values of these displacements are shown plotted as points using open symbols for Stations C and E. The vertical solid lines connecting these points indicate the difference between measured values at these two stations. The solid circular symbols are the average of these two values at each measurement point. Presenting the data in this way seems reasonable because the stratigraphic cross section used in the analyses is viewed as an average of conditions existing at Stations C and E.

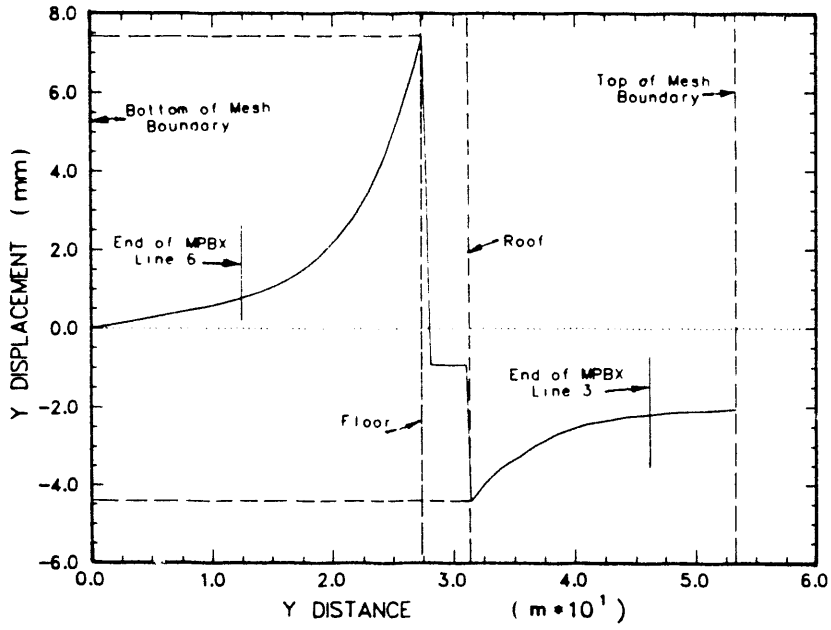

Figure 6. Vertical Displacements Along Vertical Centerline of the Demonstration Drift

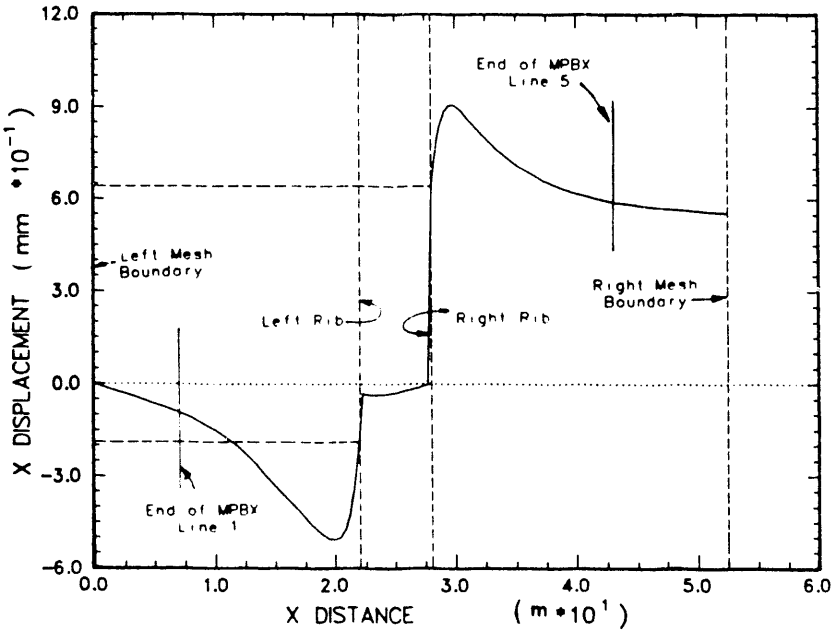

Figure 7. Horizontal Displacements Along a Line Through MPBX Lines 1 and 5

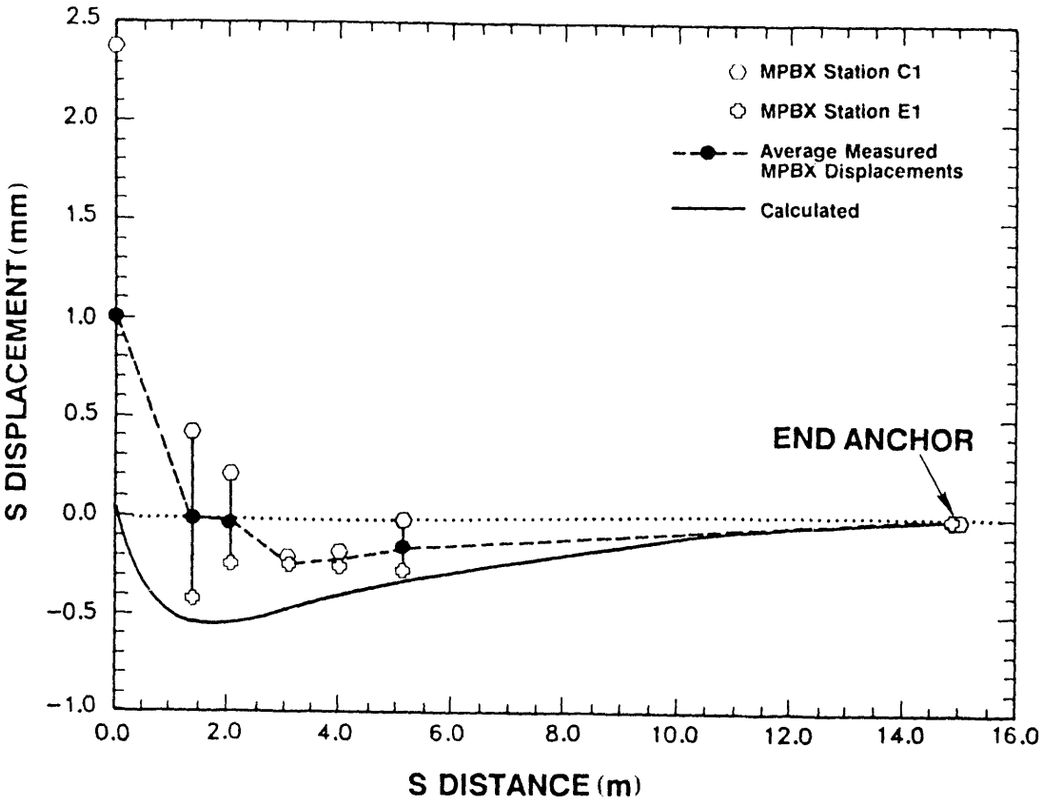

Figure 8. Displacements Along MPBX Line 1

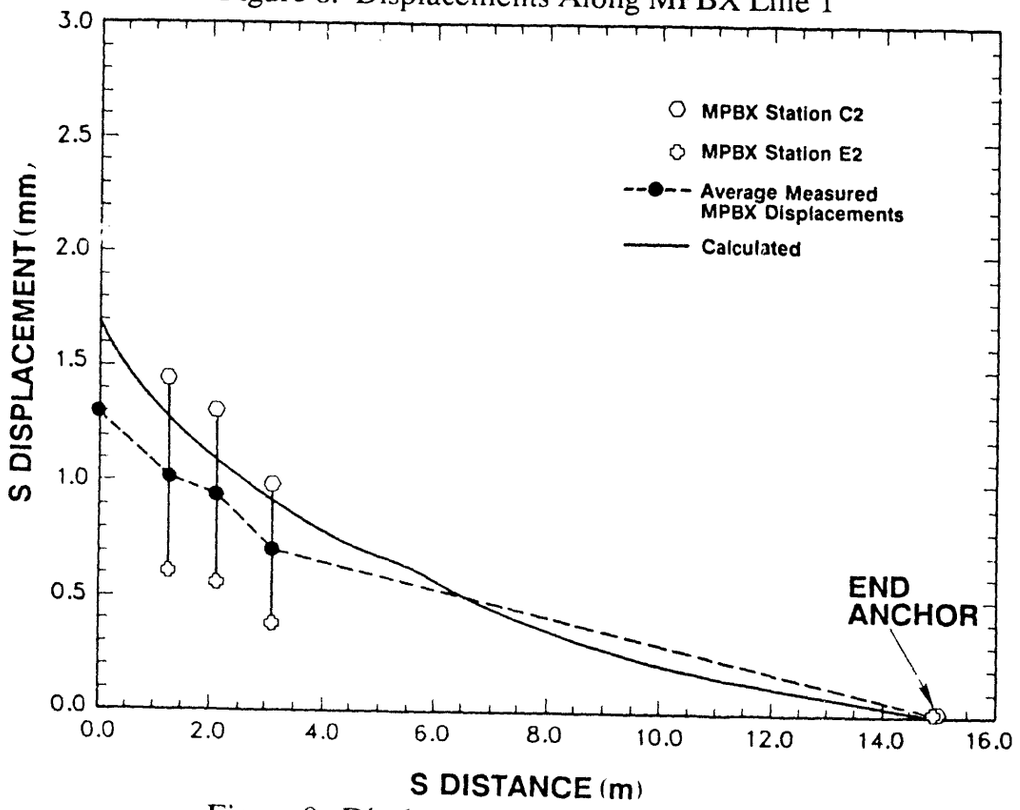

Figure 9. Displacements Along MPBX Line 2

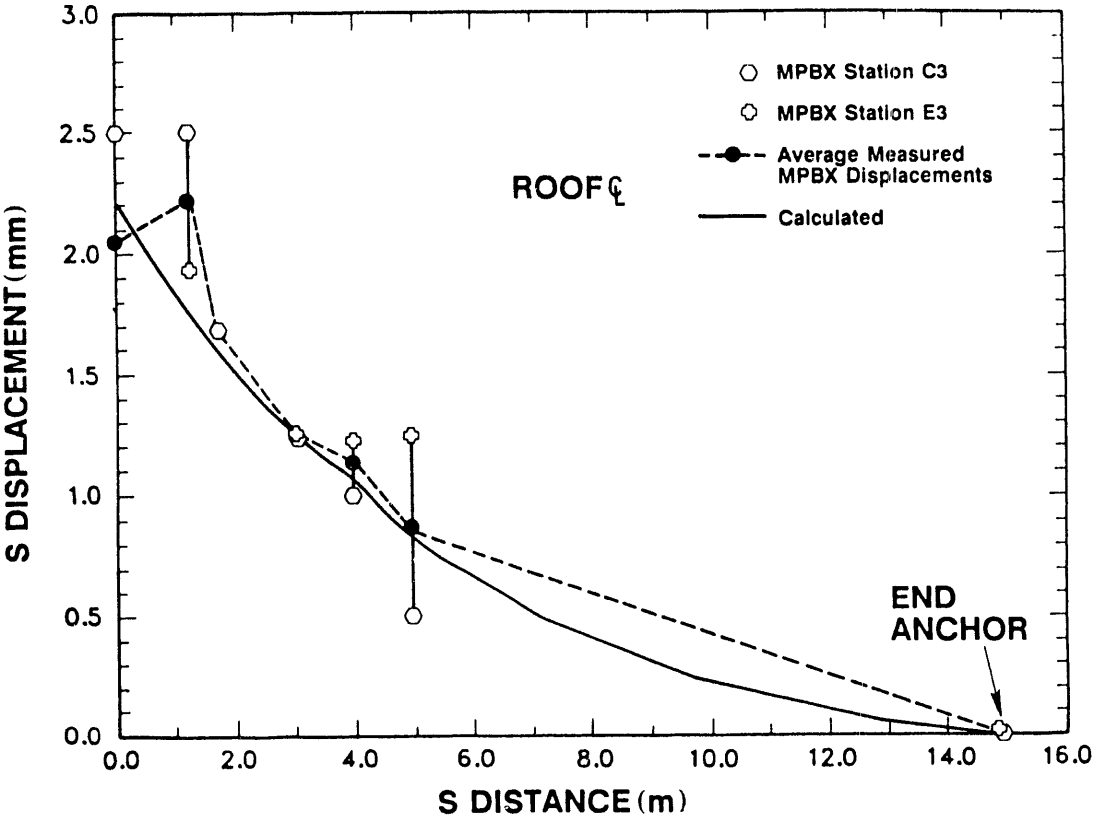

Figure 10. Displacements Along MPBX Line 3

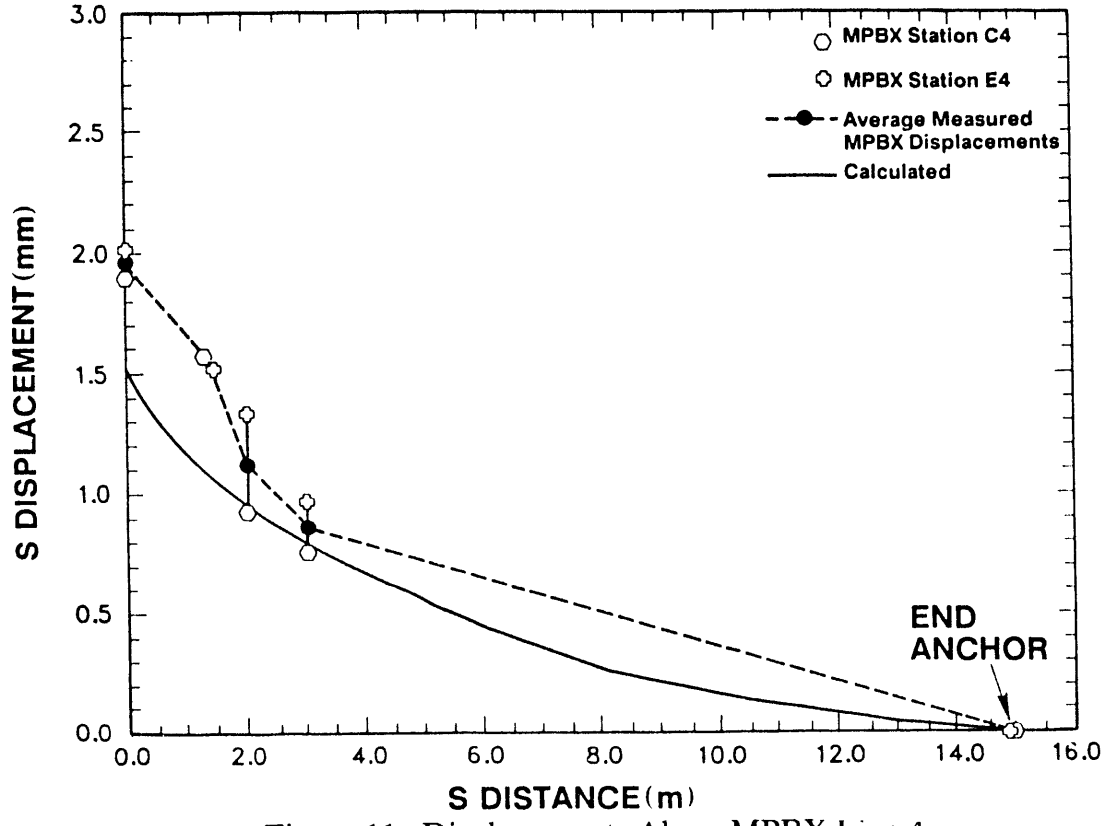

Figure 11. Displacements Along MPBX Line 4

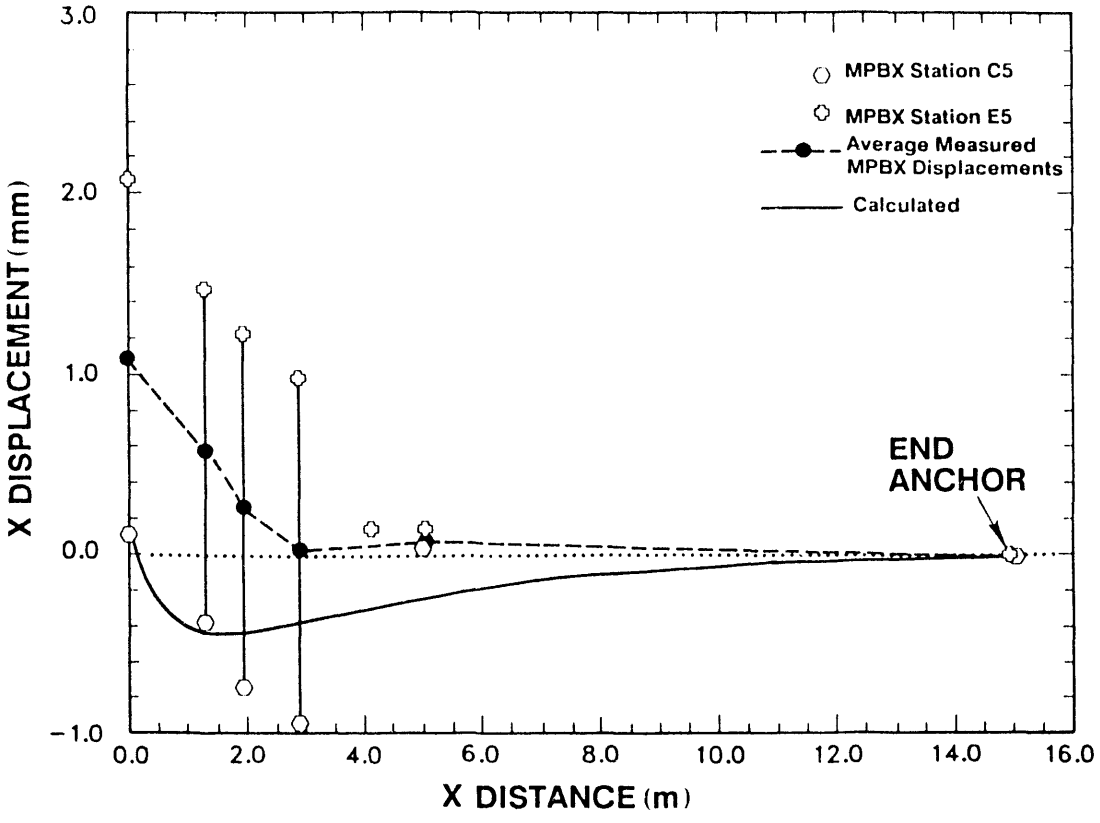

Figure 12. Displacements Along MPBX Line 5

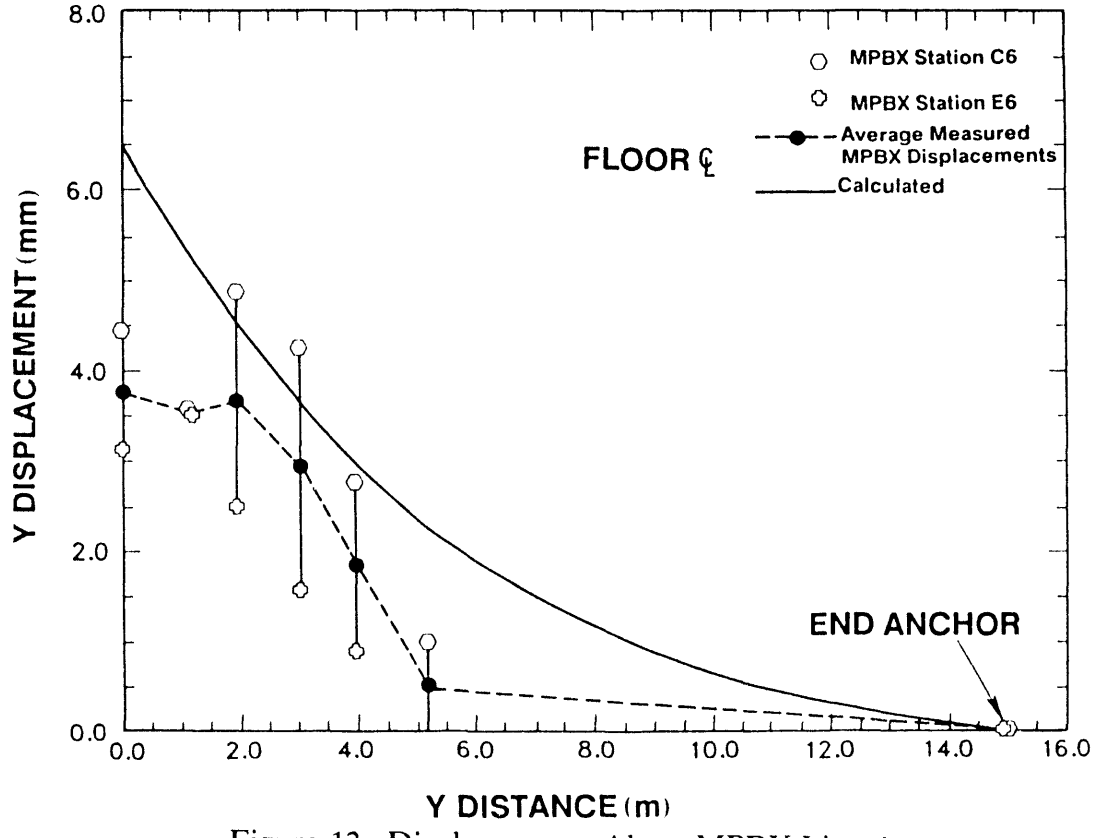

Figure 13. Displacements Along MPBX Line 6

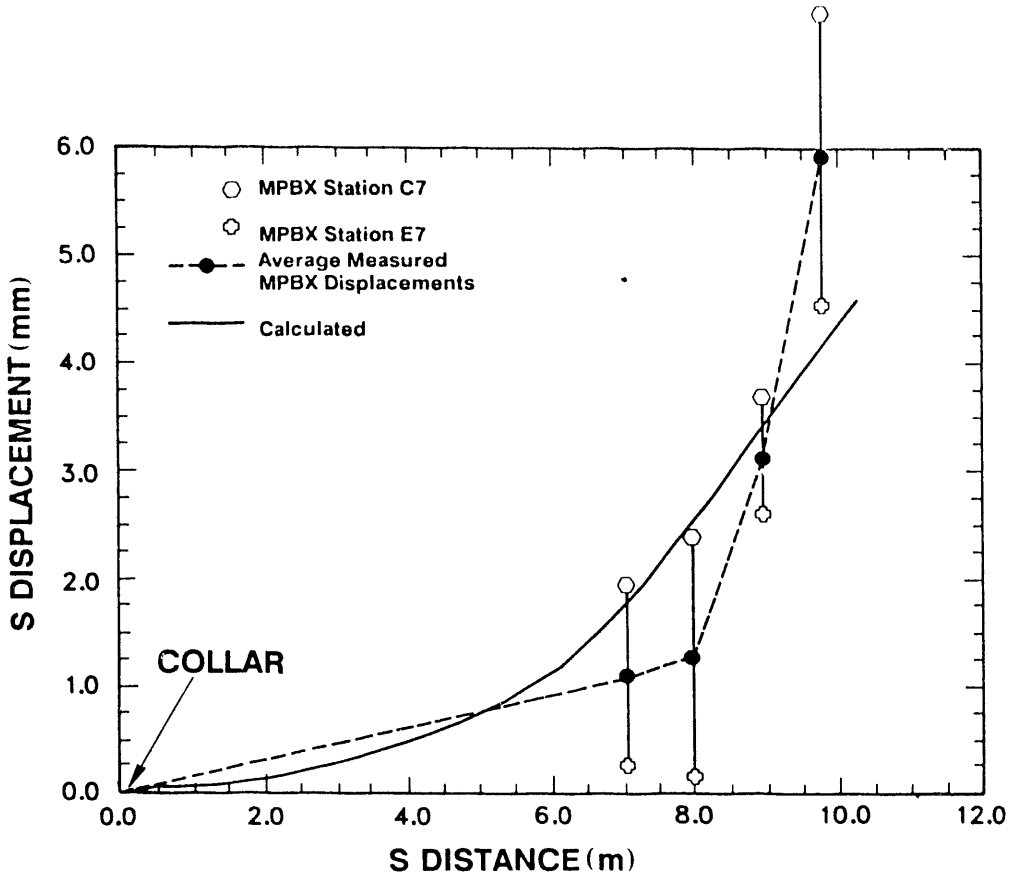

Figure 14. Displacements Along MPBX Line 7

An exception to this is the plot of displacements along MPBX Line 7 where the displacements are plotted relative to the collar installed in the 12-Drift.

2.4.3 Deflectometer Angle Changes and Tangential Deviations

The method of measuring angle changes along a deflectometer borehole is illustrated in Figure 15(a). Angle changes along a deflectometer line are calculated from the finite element solution by considering rock mass displacements normal to a line coinciding with the deflectometer hole as shown in Figure 15(b), where the h = 0.76 m dimension is the distance between sampling points along the borehole. The angles R_i and R_{i-1} are calculated using the following equations:

$$R_i = \tan^{-1}[(v_{i+1} - v_i)/h] \qquad 2 \le i \le 23$$

$$R_{i-1} = \tan^{-1}[(v_i - v_{i-1})/h]$$

where i is the i^{th} sampling point and h is the sampling interval. The angle change between two intervals is then

$$DA_i = R_i - R_{i-1} .$$

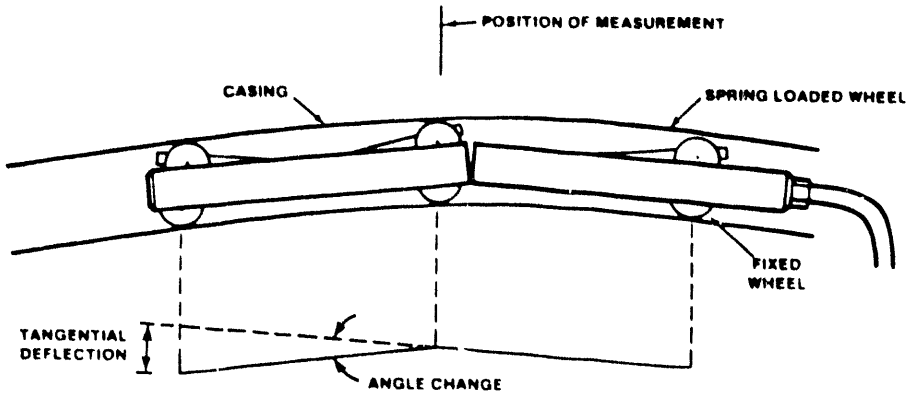

(a) Schematic of Borehole Deflectometer in Casing (Reference 2)

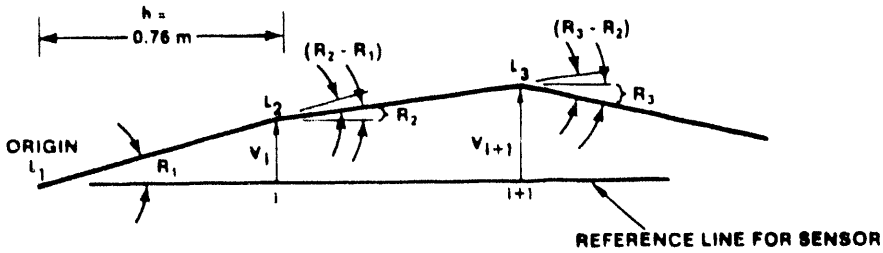

$DA_i = (R_i - R_{i-1})$, WHERE $DA_1 = 0$ AND $2 \leq i \leq 23$

$$D_n = \sum_{i=1}^{i=n-1} (L_i - L_{i-1}) \times (R_i - R_{i-1}) \quad 2 \leq n \leq 23$$

(b) Schematic Showing Geometry Defining Angle Changes and Tangential Deviations

Figure 15. Method of Measuring and Computing Angle Changes and Tangential Deviations Along Deflectometer Boreholes

A positive angle change in Figure 15 indicates a decrease in the angle of the borehole measured from the horizontal direction. Because the angle changes are small, the tangential deviation, dD, may be calculated as

$$dD = h \times dA \text{ and } D_n = \sum_n dD, \quad 2 \le n \le 23 .$$

Figures 16 and 17 are plots comparing the tangential deviations computed from the finite element solution with those computed from deflectometer measurements taken in Boreholes 1 and 4 at Stations B and F, respectively. An attempt was made to compare displacements normal to the boreholes calculated from the finite element solution with those calculated from borehole deflectometer measurements. The comparison was unsatisfactory because the values of normal displacements calculated from measurements of angle changes were sensitive to (1) the measured initial angles, which could vary by an order of magnitude, and (2) the sign of this initial angle.

2.4.4 Borehole Stresses

Figures 18 and 19 are plots of calculated stresses normal to the lines coinciding with deflectometer Lines 1 and 4. These stress components are calculated in a coordinate system where the s-axis coincides with the direction of the deflectometer line beginning at the surface of the 12-drift, and the n-axis is normal to this line.

The stresses indicated are the net stresses or stress changes obtained by subtracting the stress states at Time 2 from those at Time 3.

2.5 Summary of Previous Calculations

In this section the results of calculations reported in a letter memorandum dated June 29, 1984, (Appendix A) and those of the intermediate set (May 1986) are summarized. The results of all drift convergence calculations, including the latest, are listed in Table 4.

2.5.1 Calculations of June 29, 1984

The finite element mesh used in this set of calculations is shown in Appendix A (Figure A.1). Numbers indicate nodal points in the mesh, which correspond to displacements in the accompanying tables. Note that the roof of the Demonstration Drift is flat except for small corner radii. The Demonstration Drift is located completely in the densely welded tuff. The top of the basal vitrophyre is indicated by the heavy line sloping down from left to right in the figure. There is no rubble zone defined.

Boundary conditions are the same as those used in the current set of calculations except that the right vertical boundary is fixed against horizontal displacement. In situ stresses were selected as -8 MPa vertical and -2 MPa horizontal. The material properties used are listed in Table 5.

Vertical and horizontal convergences of the Demonstration Drift for these calculations are shown in Line 1 of Table 4. These values are obtained by subtracting the displacements at Time = 2 from those at Time = 3 shown in the tables of the appended letter memorandum.

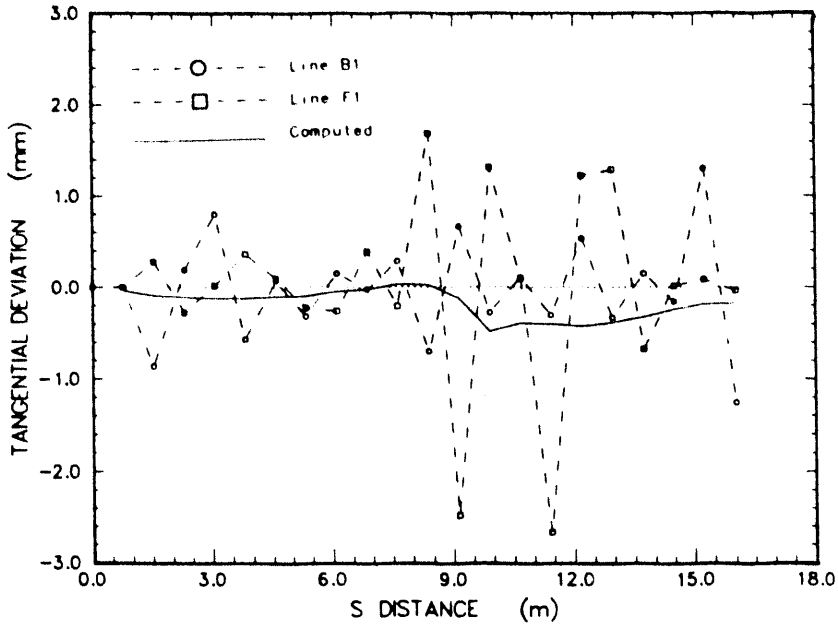

Figure 16. Computed and Measured Tangential Deviations Along Deflectometer Lines B1 and F1

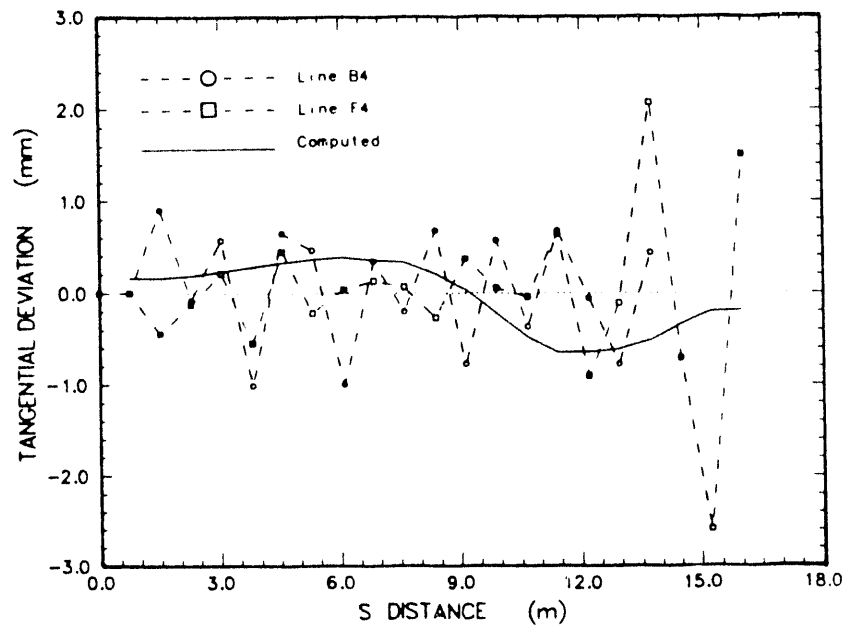

Figure 17. Computed and Measured Tangential Deviations Along Deflectometer Lines B4 and F4

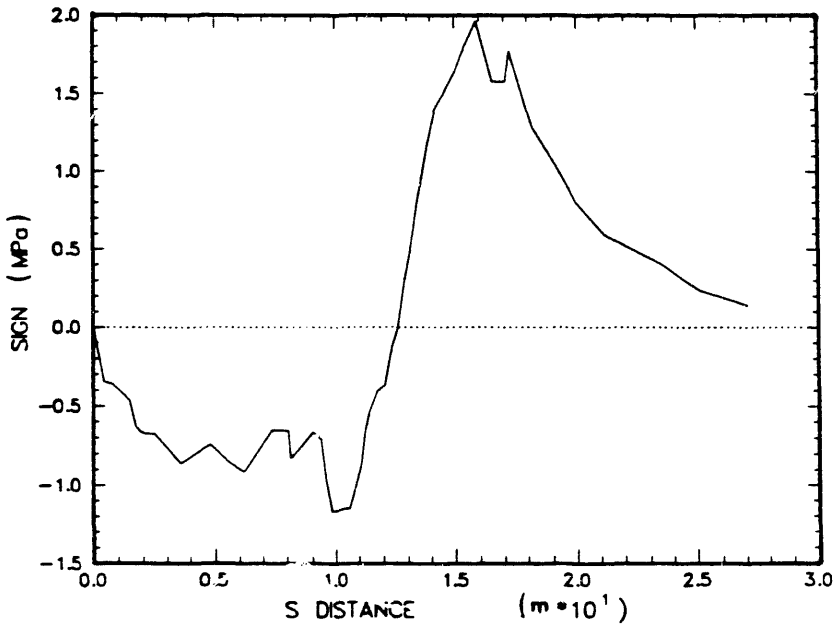

Figure 18. Computed Stresses Normal to Deflectometer Line 1

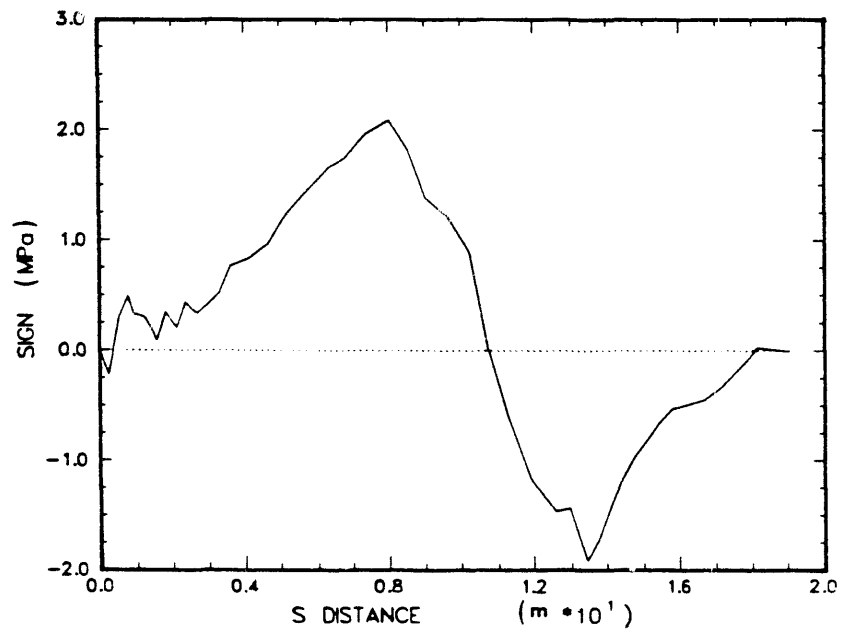

Figure 19. Computed Stresses Normal to Deflectometer Line 4

Table 4

G-Tunnel Mining Experiment--Summary of Computed Drift Displacements

Problem Specification	Vertical Displacements at Centerline of Demonstration Drift (mm)			Horizontal Displacements at Midheight of Demonstration Drift (mm)		
	Floor	Roof	Vertical Convergence	Left Rib	Right Rib	Horizontal Convergence*
Geometry and Stratigraphy of June 29, 1984	3.10	-4.39	7.49	-0.09	0.45	-0.54
Linear Elastic--Old Props. Horiz In situ Stress = -2 MPa	8.75	-5.85	14.60	-0.74	0.75	-1.49
Linear Elastic--Old Props. Horiz In situ Stress = -4 MPa	8.45	-5.82	14.27	-0.34	0.03	-0.37
Linear Elastic--New Props. Horiz In situ Stress = -2 MPa	6.00	-5.12	11.12	-0.54	0.36	-0.90
Compliant Joint--New Props.	5.29	-4.03	9.32	0.0	-0.20	0.20
Linear Elastic (Zimmerman Props.) Horiz In situ Stress = -2 MPa	7.40	-4.60	12.00	-0.19	0.63	-0.82

* Convergence (inward movement) is positive.

Table 5

Rock Mass Mechanical Properties of Geologic Units
Used in the Calculations of June 29, 1984*

Geologic Unit	Young's Modulus, E (MPa)	Poisson's Ratio, ν
C (moderately welded tuff)	12,000	0.21
B (densely welded tuff)	16,000	0.21
Volcanic Breccia (rubble)	--	-
Basal Vitrophyre	4,000	0.21
Tunnel Bed Tuff	4,000	0.28

*From personal communication with R. M. Zimmerman.

2.5.2 Calculations of May 1986

The finite element mesh used in this set of calculations is shown in Appendix A (Figure A.3). Note the arched geometry of the Demonstration Drift and the mesh refinement in the vicinity of the drifts. Bonded slip lines were used on the boundaries of the finely and coarsely meshed regions. Boundary conditions were the same as those used in the first set of calculations.

Four variations were made in the calculations of this set:

- Perform the calculations using the material properties shown in Table 5 (referred to as "old props." in Table 4) and a linear elastic material model. In situ stresses are -2 MPa horizontal and -8 MPa vertical.
- Perform the calculation using the same properties and conditions except with a horizontal in situ stress of -4 MPa.
- Change the material properties to those listed in Table 1 (referred to as "new props." in Table 4) with a horizontal in situ stress of -2 MPa and a linear elastic material model.
- Perform the calculation using the Thomas compliant joint material model (Reference 7) and the properties of the intact rock as shown in Tables 6 and 7 with vertical joints spaced at 0.5 m, etc. In situ stresses are -2 MPa horizontal and -7.7 MPa vertical.

Table 6

Intact Rock Mechanical Properties of Geologic Units
Used in the Calculations of May 1986*

Geologic Unit	Young's Modulus, E (MPa)	Poisson's Ratio, ν
C (moderately welded tuff)	16,300	0.21
B (densely welded tuff)	26,000	0.29
Volcanic Breccia (rubble)	--	-
Basal Vitrophyre	5,900	0.21
Tunnel Bed Tuff	5,600	0.32

*From personal communication with R. M. Zimmerman

Table 7

Joint Mechanical Properties for All Units
Used in the Calculations of May 1986

Properties	Unit of Measurement
Joint Half Closure Stress	1.38 MPa
Maximum Normal Joint Closure Constant	-.000127 m
Joint Shear Stiffness	1.0×10^7 MPa
Joint Friction Coefficient	0.8
Joint Cohesion	0.0 Mpa
Joint Shear Reduction Factor	0.0
Average Joint Set Angle	90. deg
Average Joint Spacing	0.5 m
Angle Probability Exponent	1000.

The results of these four calculations are listed on Lines 2-5 in Table 4. With reference to the linear elastic calculations, vertical displacements were affected most by a change in the elastic moduli while horizontal displacements were more sensitive to changes in the horizontal in situ stress. All linear elastic calculations predict a horizontal divergence of the drift ribs. The compliant joint model analysis does, however, predict convergence, which is the apparent sense of displacements measured (0.2 mm calculated versus 5.3 mm measured). With the compliant joint model, the vertical convergence is also smaller than that predicted by the linear elastic models, probably because the value of Young's modulus used in the compliant joint model is considerably higher (26,000 MPa versus 16,000 MPa) than those used in the linear elastic model.

2.5.3 Observations of Results of Previous Calculations

Horizontal displacements obtained by the use of linear elastic models all predict divergence of the ribs of the Demonstration Drift, contrary to measured convergences. The compliant joint model predicts horizontal convergence of the ribs; however, the displacements are smaller than those measured (0.2 mm calculated versus 5.3 mm average measured). It is possible that part of the measured convergences may result from any combination of the following mechanisms: (1) dilatation of joints in the ribs, (2) block movement along major fractures and faults, (3) slabbing of the ribs, and (4) in the blast damage zone, rock mass readjustments, which were not characterized nor considered in this analysis.

The dominant difference between the linear elastic model and the compliant joint model is that of the anisotropy built into the analysis using the joint model. The joint model is much stiffer in the vertical direction than the horizontal.

3.0 DISCUSSION

The small number of measurements made precludes a rigorous statement regarding the validity of the approach to analyze the experiment. As discussed by Costin and Bauer (Reference 1), gage installation was made at a time when approximately two-thirds of the deformation may have already occurred. The general trends in displacements predicted by the analyses correlate somewhat with those measured. Major fractures and changes in stratigraphy along the drift probably affect the measured results yet are not included in the analysis. The use of a so-called average or generic cross section could not be expected to model all conditions. In future calculations, each measurement station could be modeled independently, or alternatively, a three-dimensional model may be used to investigate the nature and extent of out-of-plane displacements resulting from motion along fault lines inclined to the axis of the drift.

Several assumptions were made in these calculations that lead to uncertainties in the results. These are (1) the use of a two-dimensional geometry and a condition of plane strain, (2) the assumption of purely elastic material behavior, (3) the assumption of mechanical properties for the rubble zone, (4) the limited dimensions of the finite element mesh and assumed boundary conditions, (5) the assumption of constant in situ stresses throughout the region of the mesh, (6) the lack of provisions for modeling the ground support system, and (7) the inability to simulate the mining sequence of the Demonstration Drift and gage emplacement by 2-D calculations.

The first of these assumptions is valid only near the mid-point of a very long drift where out-of-plane displacements are zero, whereas the drift modeled was relatively short; the possibility of drift end effects cannot be discounted. Two-dimensional analysis does not permit the modeling of faults or fractures inclined to the direction of the drift nor variations in stratigraphy along the drift. Only those discontinuities perpendicular to the plane of analysis may be modeled, assuming that an appropriate material model is used.

The second of the above assumptions limits the model to homogeneous, isotropic, and linear elastic materials. The presence of faults or joints and the potential for their localizing displacements and/or imparting anisotropy to the rock mass may violate the requirements of the assumed behavior. The jointed rock material model with nonlinear behavior is available in JAC, but insufficient information about joint characteristics was available to use this model. To this end, it should be noted also that the compliant joint model does not allow for tensile stresses to accumulate. This is a difference between it and the elastic model used. The compliant joint model also allows for anisotropic material response to be modeled by prescribing direction to the joints. It must be added, however, that the displacements measured are so small that one may not necessarily be able to discern between the results using a more sophisticated model and those presented here; thus, to use this type of experiment to discriminate between models may be misleading.

No information was available on the properties of the rubble layer; hence, a Young's modulus approximately one-half that of the basal vitrophyre was used (Table 1).

An attempt was made to assess the modeling errors resulting from limiting the extent of the finite element mesh and assuming boundary conditions for a problem of actual semi-infinite extent. A solution obtained using a pressure traction on the right vertical boundary was compared to one where horizontal displacements were constrained to zero along that boundary. Figures 20 (a) and (b) show plots of vertical displacements from the top to the

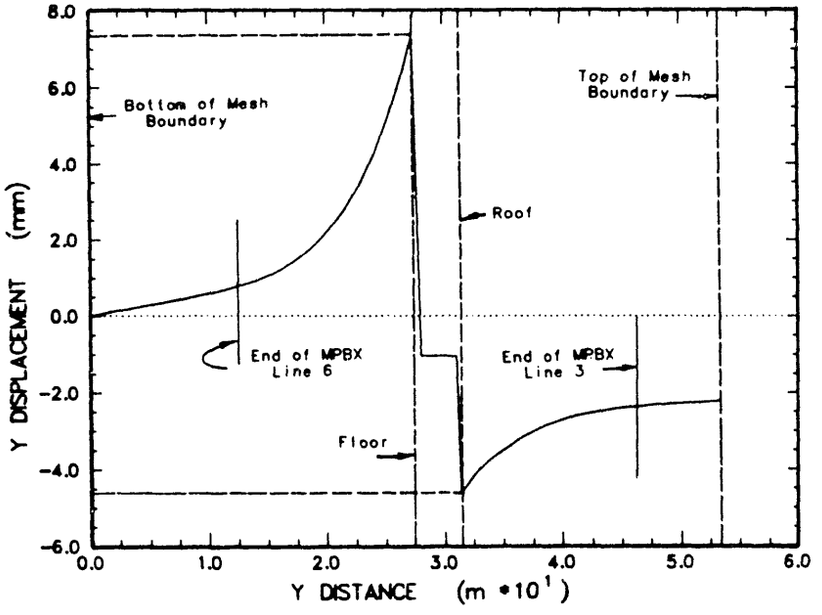

(a) Pressure on the Right Vertical Boundary

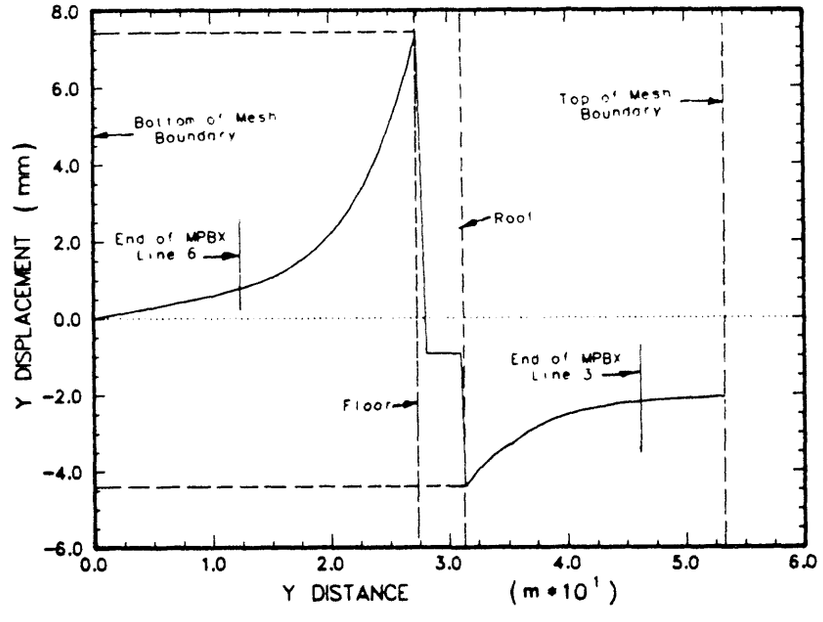

(b) Zero Displacement on the Right Vertical Boundary

Figure 20. Comparison of Solutions for Vertical Displacements for Different Boundary Conditions at the Right Vertical Mesh Boundary

bottom of the mesh along a vertical centerline through the Demonstration Drift. Figure 20(a) is the same as Figure 6, repeated here for comparison. In each figure the distance between the two medium-dashed horizontal lines is the predicted drift closure after excavation. It can be seen that the total vertical closure of the drift is approximately 12 mm in Figure 20(a) and 12.5 mm in Figure 20(b), indicating an effect from the right boundary on the order of 4%. Thus, it could be concluded that boundary effects on vertical displacements are not large. It could be surmised that boundaries may have a larger effect on horizontal displacements. Hence, a comparison was made of horizontal displacements for the same two displacement and pressure boundary conditions.

Figures 21(a) and (b) are plots of the horizontal displacements along a line extending from the left to the right vertical boundaries through MPBX Lines 1 and 5. Figure 21(a) is the same as Figure 7, repeated here for comparison. A horizontal divergence (outward movement) of the room ribs (indicated by the distance between the horizontal medium-dashed lines in the figures) is predicted for both boundary conditions and is approximately 0.81 mm for the pressure boundary condition and 0.79 mm for the displacement boundary condition. Again, this difference is not large. However, the magnitudes of the displacements along MPBX Line 5 are more severely affected by the boundary conditions because the end of MPBX 5 is only about 10 m from the right vertical boundary.

Horizontal tape extensometer measurements indicate horizontal room convergences (inward motion of the room ribs) of approximately 2 mm at Station F to 10 mm at Station C (Table 2), contrary to the predicted divergences discussed above. It appears that this disparity between measured and calculated values is not explained by boundary effects.

Extending the limits of the finite element mesh would have the effect of softening the region and may result in larger displacements by reducing the effects of artificial boundaries. This problem is addressed in Reference 1 in which it was concluded that boundaries should be of the order of 10 room dimensions away from the excavated opening to minimize boundary effects. If the calculations are to be repeated, an infinite boundary condition recently implemented in JAC could be used (Reference 8).

In situ stresses vary with depth and with geologic strata. It was shown earlier that calculated values of horizontal displacements using linear elastic models were sensitive to values of the horizontal in situ stress. Future calculations should attempt to model these variations of in situ stress.

The ground support system consisted of rock bolts and wire mesh. The effect of rock bolts is to inhibit local rock movement by holding blocks together so that they may interact. The purpose of the wire mesh is to catch minor rock falls from the roof. No attempt was made in the calculations presented here to model this support system.

In Figures 22(a) and (b), horizontal displacements of the left and right ribs of the Demonstration Drift are plotted as a function of distance above the floor of the drift. It should be noted that, above the rubble zone, the predicted movement of the ribs is outward. This movement may be caused by the horizontal thrust of the arched roof against the vertical rib. The calculated stress state around the drift tends to support this contention. The horizontal and vertical components of stress around the drift opening are plotted as contours in Figures 23(a) and (b). The largest compressive horizontal stress occurs just above the springline of the arched roof. The horizontal stress is compressive along the right rib to the zero-contour, approximately 0.5 m below the springline of the roof. The zero-contour continues down to the top of the rubble zone with an indication just above the rubble zone of a small tensile zone between the rib and this contour. Through

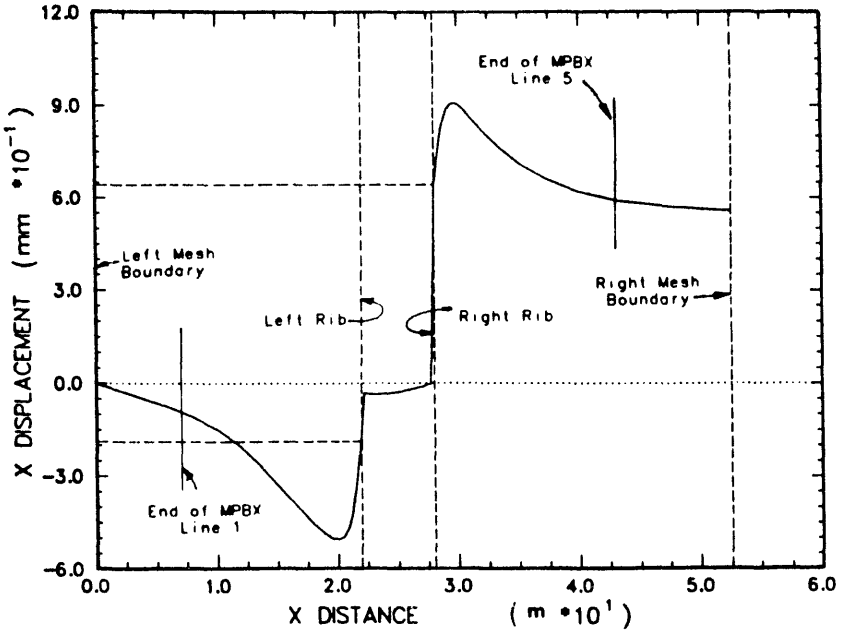

(a) Pressure on the Right Vertical Boundary

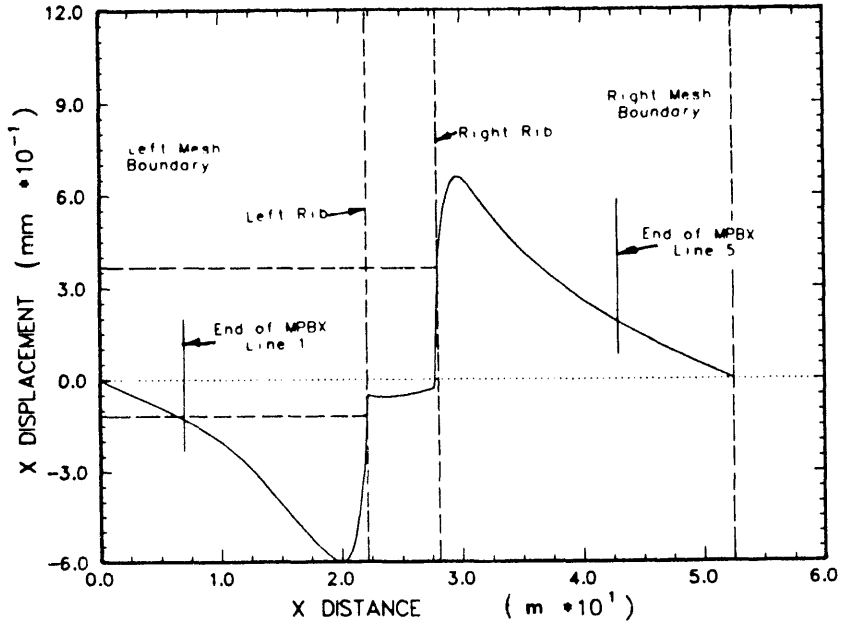

(b) Zero Displacement on the Right Vertical Boundary

Figure 21. Comparison of Solutions for Horizontal Displacements for Different Boundary Conditions at the Right Vertical Mesh Boundary

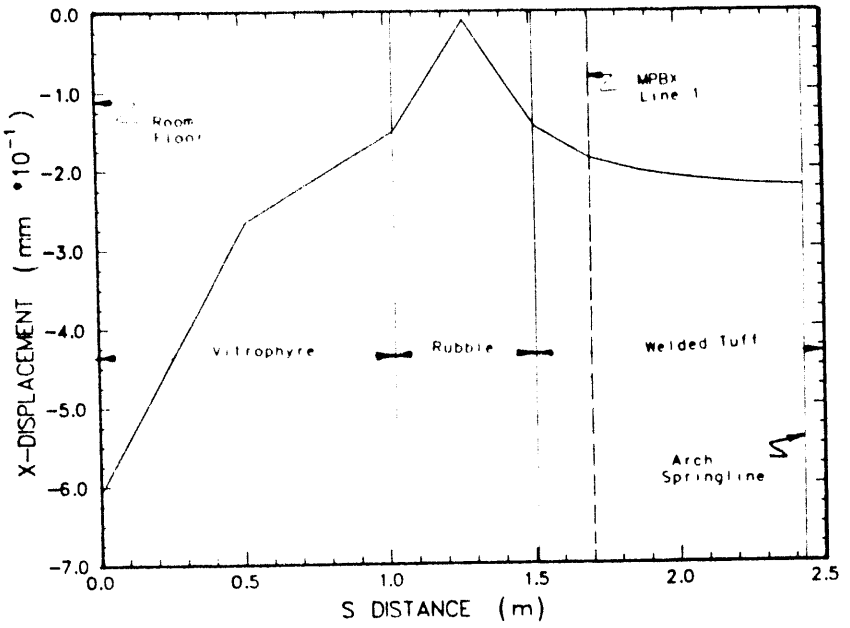

(a) Left Rib Displacements

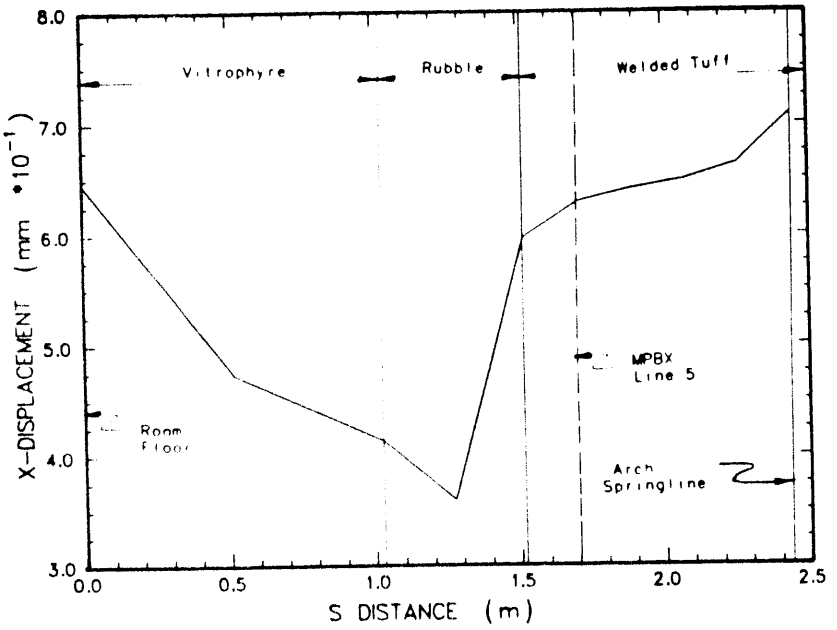

(b) Right Rib Displacements

Figure 22. Horizontal Displacements Along the Left and Right Ribs of the Demonstration Drift

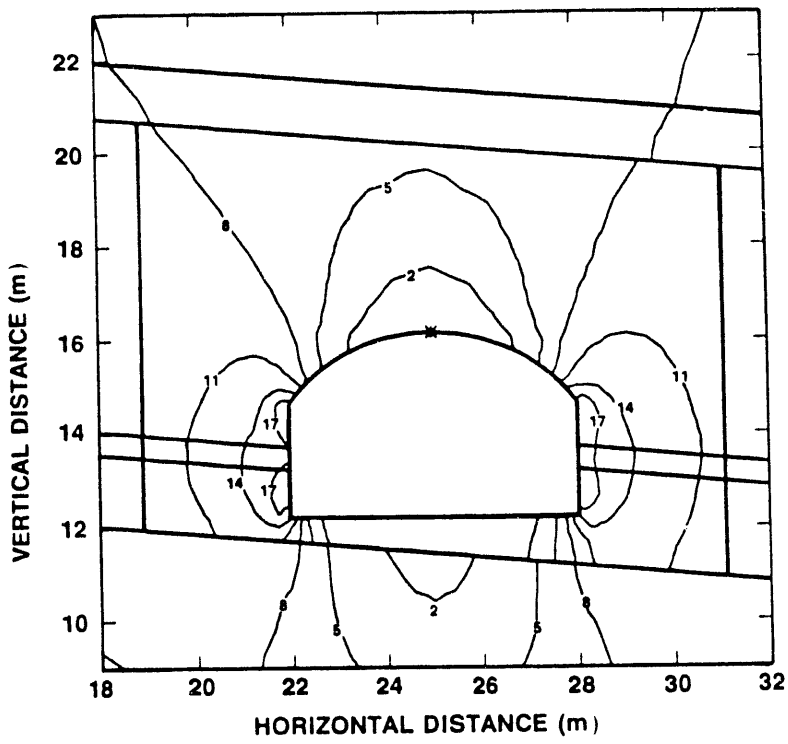

(a) Vertical Stresses

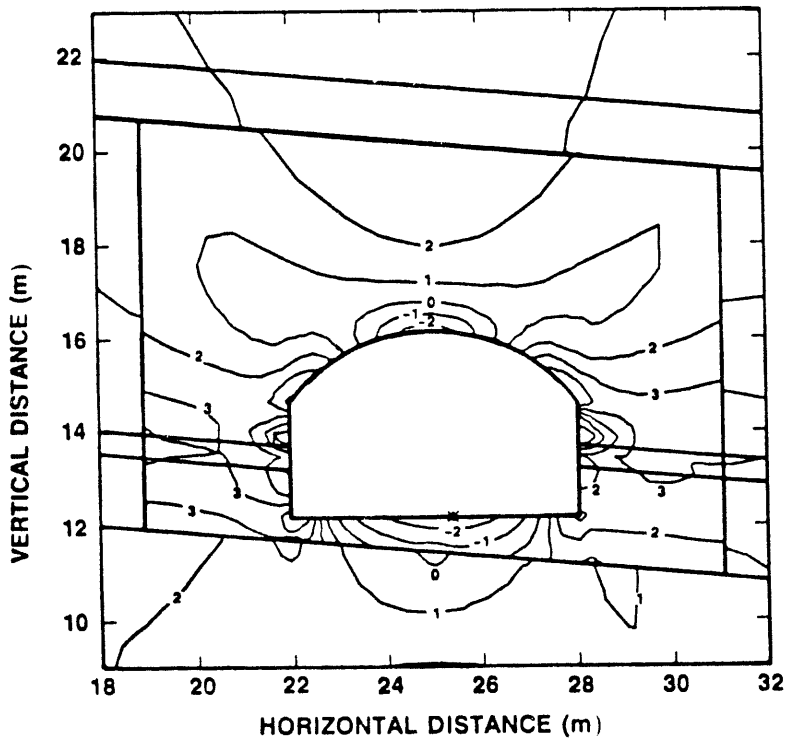

(b) Horizontal Stresses

Figure 23. Contours of Vertical and Horizontal Stresses Around the Demonstration Drift

this zone passes MPBX Line 5. A similar condition exists in the left rib. The presence of a tensile stress in the ribs admits the possibility of a tensile failure of the intact rock or a dilation of joints in this zone.

A factor of safety against a compressive shear failure of the intact rock may be calculated using the procedure given in Reference 9, where a Mohr-Coulomb criterion is used. The two parameters of this criterion are cohesion, Co, and coefficient of internal friction, μ. If the properties for Grouse Canyon welded tuff from Reference 9 are used, these parameters are Co = 16.2 MPa and μ = 0.554. The resulting contours of safety factor are shown in Figure 24, where the minimum factor of safety against compressive shear failure is approximately 2. Only very low localized tensile stresses were predicted in the analysis. Thus, one may conclude that intact rock failure is unlikely to occur based on the analysis completed.

The calculated movement of the rubble zone is inward, indicating convergence with respect to the drift ribs apparently resulting from extrusion of this softer layer. This movement, however, is not sufficient to cause a net horizontal closure or convergence of the ribs. The measured convergences may be a result of the opening of existing joints in the rib and pillar or to possible slabbing of the ribs. The possibility of some three-dimensional effect caused by movement along major fractures or fault planes cannot be dismissed.

The results of the May 1986 calculations, summarized in Table 4, show that in all linear elastic cases the horizontal displacements of the ribs are outward, indicating divergence of the drift. If jointing is considered, it is noted that this trend is reversed; however, the resulting displacements are smaller than those measured (~ 0.003 mm on the left and -0.204 mm on the right). These calculations do not include the rubble layer, which, if present, might tend to increase the magnitudes of the calculated horizontal convergence.

The effects of variation in the value of the artificial viscosity parameter used in JAC to suppress hourglassing was examined in this set of calculations. Two additional solutions were obtained with values of this parameter of 50 and 25. At the lowest value of 25, no hourglassing was evident in the solution, although hourglassing did occur when the default value of 1 was used initially. The computed displacements of the left and right ribs of the demonstration drift for three values of artificial viscosity are plotted in Figures 25(a) and (b). Note that these displacements occur at Time 3 and represent total displacements, including any displacements occurring before excavation of the drift. It can be seen that the displacements vary only about 0.1 mm for the extreme values of artificial viscosity of 100 and 25, generally increasing as the viscosity is decreased. Thus, varying the parameter over this range is of little consequence for the results predicted. At the MPBX locations, where the tape extensometer measurements of drift convergence were made, the displacements are negative or outward from the left rib and positive or outward from the right rib. The sense of these computed displacements does not change with a change in the viscosity; therefore, the effects of artificial viscosity do not explain the disparity between measured and computed horizontal drift closures. The results are consistent with the values of horizontal displacements shown in Table 4, where the linear elastic calculations all predict drift divergence.

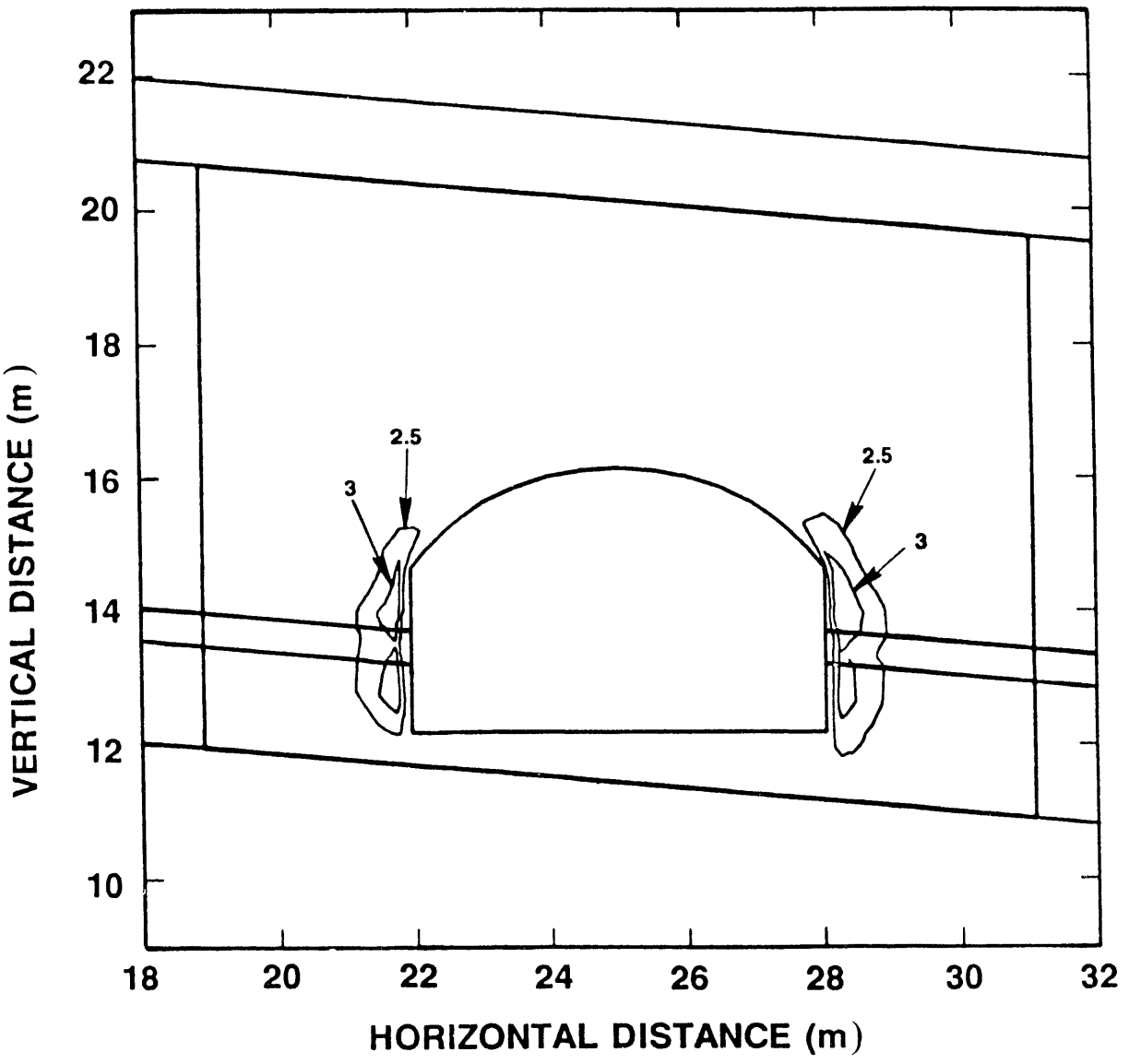

Figure 24. Contours of Factor of Safety Against Intact Rock Failure Around the Demonstration Drift

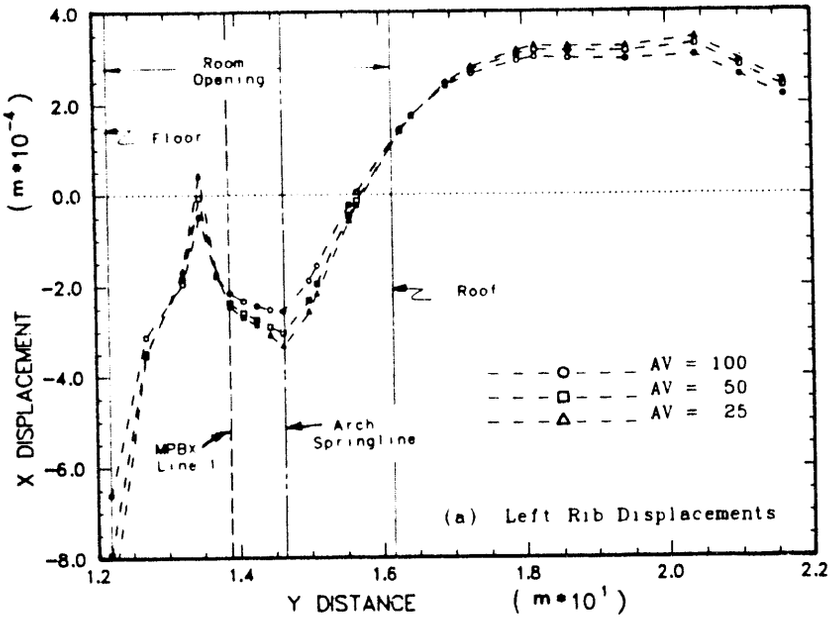

(a) Left Rib Displacements

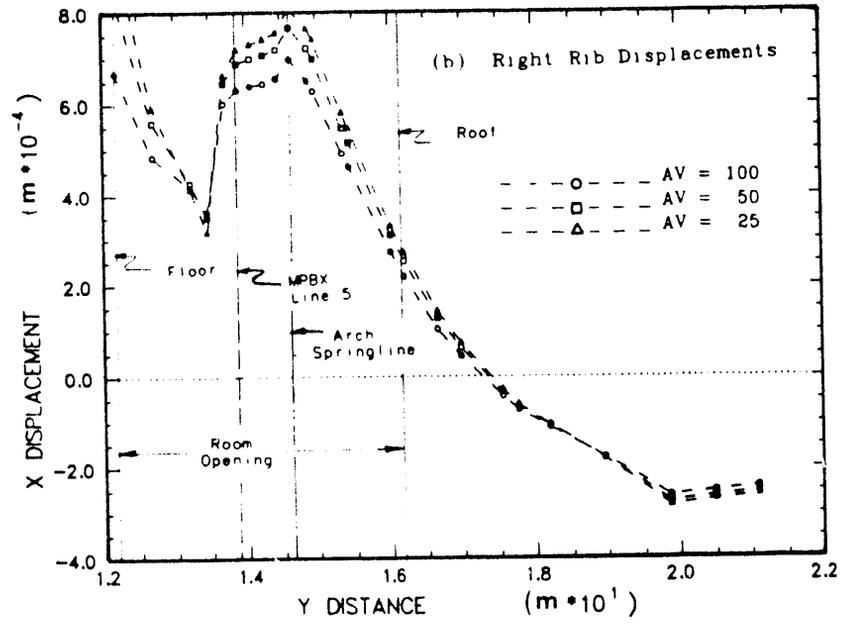

(b) Right Rib Displacements

Figure 25. Effects of Artificial Viscosity on Demonstration Drift Rib Displacements

An additional question of numerical accuracy of the calculations seems to arise as a result of the above discussion. From Table 4, the calculated vertical closure or convergence of the Demonstration Drift varies from 9 to 14 mm depending on values of elastic material moduli, magnitude of in situ stresses, and jointing. The variation of Young's modulus appears to be the most significant parameter influencing the vertical displacements. What is apparent is the sensitivity of the values of horizontal displacements to changes in the above parameters. These displacements are at least an order of magnitude smaller than the vertical displacements, and this difference raises the question of whether the results are lost in the noise of the solution.

In light of the above discussion and the implied uncertainties, it is necessary to address trends in behavior rather than magnitudes of computed displacements and stresses. Certain conclusions may be drawn by observation of these trends.

It can be seen by comparing both vertical and horizontal convergences obtained from tape extensometer and MPBX measurements in Table 2 that the MPBX measurements are approximately one-half (or less) of those obtained by tape extensometer. This indicates that the tape extensometer measurements are probably reflecting, to a great extent, local block movement within a short distance of the opening (probably < 1 m). Whereas, the MPBX measurements, which do not readily sense this skin effect around the opening because of the way the anchors are emplaced in the rock, reflect predominantly the rock mass response from excavation loads only. Another factor affecting MPBX measurements could be that the deep anchor moved.

4.0 CONCLUSIONS

Preliminary calculations have been completed in support of the welded tuff mining experiment in G-Tunnel. Results show reasonable agreement between computed results and measurements if displacement trends rather than absolute magnitudes are considered. The difference between measurements of the horizontal drift closure and computed results has yet to be resolved. Calculations using linear elastic models are consistent in that horizontal room divergence is predicted in all cases. Speculation is that the anomaly results either from three-dimensional effects, such as movement along major fractures or faults inclined to the direction of the drifts, or from dilation of joints in the rib and pillars.

A comparison of drift convergences measured by tape extensometer and by MPBXs shows that MPBXs reflect rock mass response to excavation loads only. Tape extensometers measured approximately twice as much magnitude of displacements as the MPBXs, because these measurements also reflect local block movements at the opening surface.

The rubble zone passing through the Demonstration Drift causes abrupt discontinuities in the displacements of the room ribs, showing a tendency to extrude from between the densely welded tuff (Unit B) and the basal vitrophyre layers. This extrusion at the softer layer may also contribute to the development of small tensile zones in the ribs just above the rubble layer.

Slabbing of the ribs could be considered as a possible cause of the measured horizontal convergence of the room ribs, although intact rock failure is not predicted by the calculations. The opening of subvertical joints in the rock mass adjacent to the ribs appears to be as likely. The effect of either of these mechanisms should be captured in future calculations where the use of material models for jointed rock appears to be warranted.

It is recommended that the boundaries of the finite element mesh be extended in any future calculations. The distance of 10 room dimensions away from the excavated opening would minimize the effects of artificial boundaries. As an alternative, an infinite boundary condition may be imposed to remove the boundary effects.

The disparity between borehole deflectometer measurements and calculated results may be the result of block movement in the rock mass or from the questionable borehole deflectometer measurements. Further comparison between measured and computed results is unwarranted unless steps are taken to model this behavior and improve the measurement (deflectometer) technique.

MPBX measurements were limited to a total of 14 subparallel lines of data collection (with a limited number of data points on each line), and comparison with computed results is not statistically meaningful, particularly with the small number of data points for a given orientation. If possible, more measurement lines of data collection and data points would be desirable.

5.0 REFERENCES

1. L. S. Costin and S. J. Bauer, "Preliminary Analyses of the Excavation Investigation Experiments Proposed for the Exploratory Shaft at Yucca Mountain, Nevada Test Site," SAND87-1575, Sandia National Laboratories, Albuquerque, NM, June 1989. (NNA.881202.0209)

2. R. M. Zimmerman, R. A. Bellman, Jr., K. L. Mann, and D. P. Zerga, "G-Tunnel Welded Tuff Experiment Preparations," SAND88-0475, Sandia National Laboratories, Albuquerque, NM, January 1991. (NNA.901127.0256)

3. R. M. Zimmerman, R. A. Bellman, Jr., K. L. Mann, D. P. Zerga, and M. Fowler, "G-Tunnel Welded Tuff Mining Experiment Data Summary," SAND88-0474, Sandia National Laboratories, Albuquerque, NM, April 1990. (NNA.900214.0309)

4. J. H. Biffle, "JAC -A Two-Dimensional Finite Element Computer Program for the Non-Linear Quasistatic Response of Solids with the Conjugate Gradient Method," SAND81-0998, Sandia National Laboratories, Albuquerque, NM, April 1984. (HQS.880517.2257)

5. R. M. Zimmerman, R. E. Finley, "Summary of Geomechanical Measurements Taken in and Around the G-Tunnel Underground Facility, NTS," SAND86-1015, Sandia National Laboratories, Albuquerque, NM, May 1987. (NNA.870526.0015)

6. D. P. Flanagan and T. Belytschko, "A Uniform Strain Hexahedron and Quadrilateral with Orthogonal Hourglass Control," International Journal for Numerical Methods in Engineering, 1982, Vol. 17, pp. 679-706. (NNA.900319.0053)

7. R. K. Thomas, "A Continuum Description for Jointed Media," SAND81-2615, Sandia National Laboratories, Albuquerque, NM, April 1982. (HQS.880517.2785)

8. M. Stern and L. M. Taylor, "A Coupled Boundary Integral and Finite Element Formulation for Nonlinear Halfspace Problems," SAND86-1902, Sandia National Laboratories, Albuquerque, NM, December 1986. (NNA.900129.0543)

9. R. L. Johnson and S. J. Bauer, "Unit Evaluation at Yucca Mountain, Nevada Test Site: Near-Field Thermal and Mechanical Calculations Using the SANDIA-ADINA Code," SAND83-0030, Sandia National Laboratories, Albuquerque, NM, May 1987. (NNA.891019.0277)

APPENDIX A

date June 29, 1984

to S. J. Bauer and R. Zimmerman, 6313

from R. L. Johnson, 1524

subject Two-Dimensional Calculations in Support of "Mineby Experiment"

Finite element calculations have been completed for the subject task and preliminary results were transmitted to S. J. Bauer on June 28, 1984. Geometry, material properties and boundary conditions were used as specified in your memo of June 6, 1984. A linear elastic model in the computer code JAC was used in the calculations. Displacements and stresses in the rock mass were computed for the following conditions.

1. In-Situ state (T=1), prior to any excavation
2. Excavation of Drift 12 (T=2)
3. Excavation of the Demonstration Drift (T=3)

Results of the calculations were presented in the form of displacement versus distance plots (SPLOTs) along the lines specified in your memo, i.e., along the vertical centerline of the demonstration drift and along lines A and B as shown in the attached Figures 1 and 2, and contours of vertical (SIGY), horizontal (SIGX) and shear stresses (SIGXY) for the region and for the individual drifts. Units of displacements and distance in the SPLOTs are meters, stresses in the contour plots are in MPa.

Tabulated displacements in millimeters (mm) at the mid-dimensions of the two drifts and at other nodal points identified in Figures 1 and 2 are shown in the attached tables for excavation conditions 2 and 3. Displacements prior to excavation are all zero and stresses are equal to the in-situ stresses.

Copy to:
1524 W. Sullivan
6310 T. Hunter
6313 J. Tillerson
6313 L. M. Ford
6313 A. Stevens
6330 J. T. Henderson (NNWSICF)

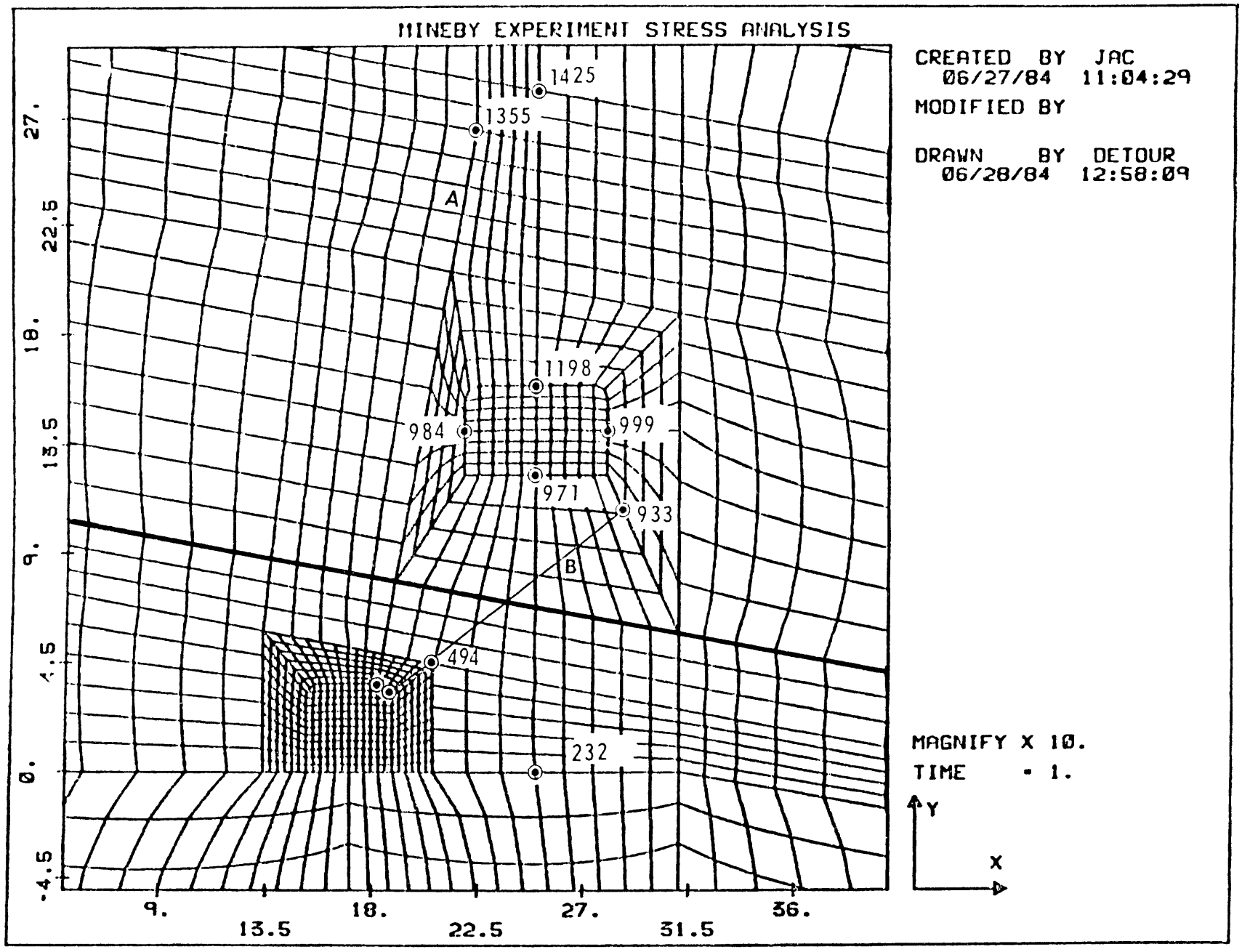

Figure A.1 Finite Element Mesh Showing Both Drifts
(Calculations of June 29, 1984).

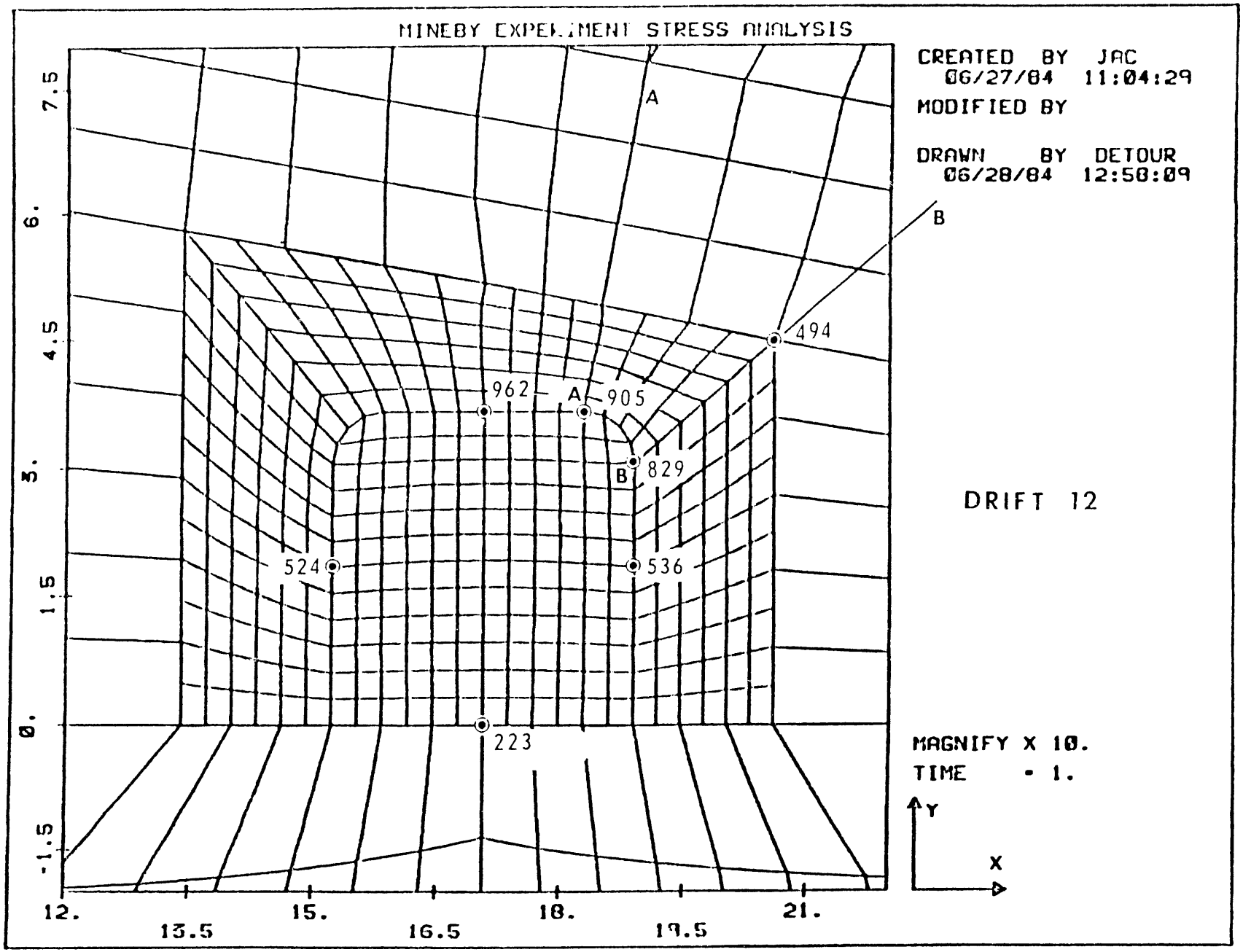

Figure A.2 Finite Element Mesh in Region of Drift 12
(Calculations of June 29, 1984)

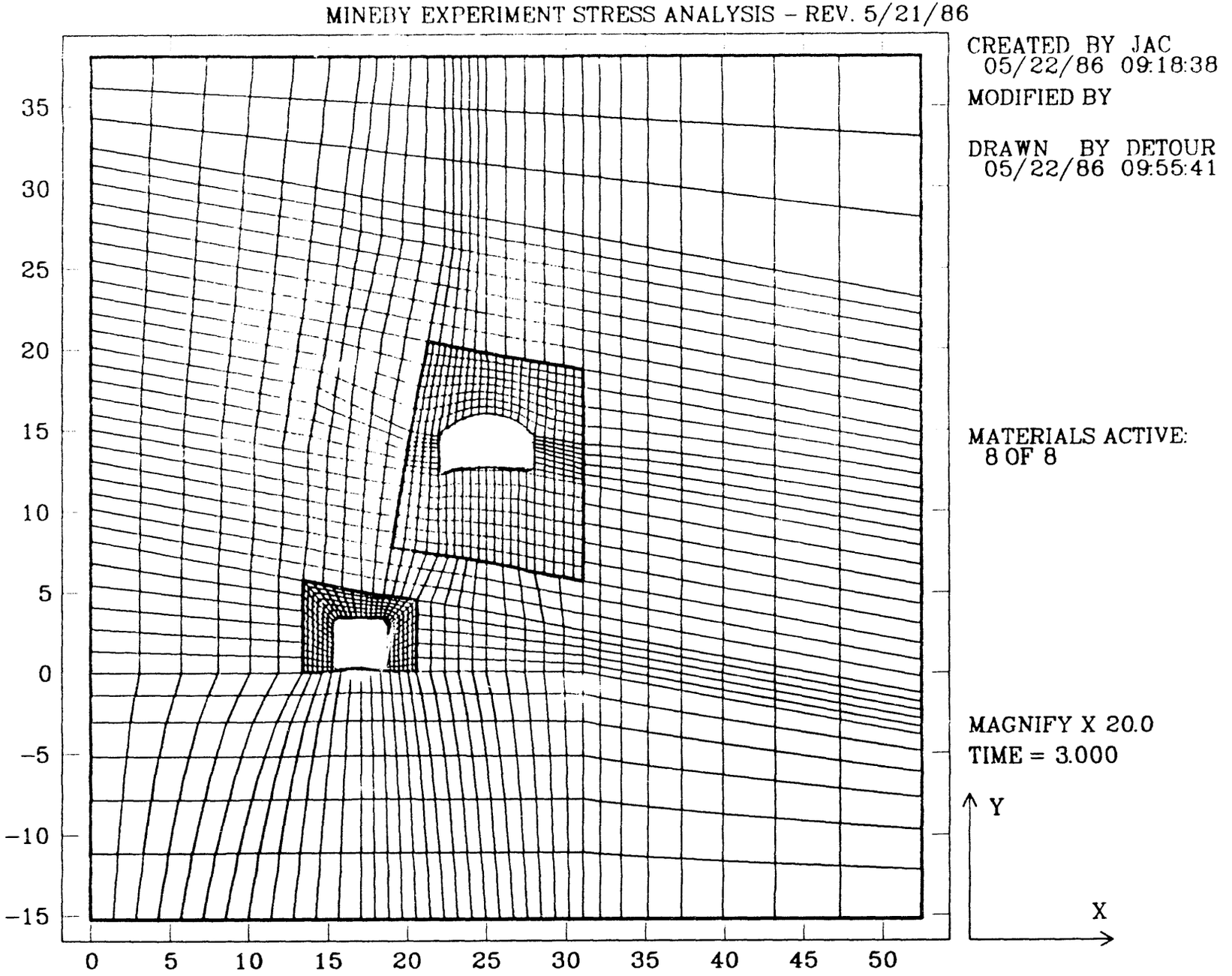

Figure A.3 Finite Element Mesh After Excavation of Both Drifts (Calculations of May 1986).

Table A.1

DISPLACEMENTS AFTER EXCAVATION OF DRIFT 12 (T=2)

Location	Node	x m	y m	Ux mm	Uy mm
Centerline Floor Drift 12	223	17.07	0.0	0.034	6.875
	232	25.00	0.0	0.102	-0.373
	494	20.60	4.48	-0.107	-1.309
Midheight Rib Drift 12	524	15.24	1.83	1.119	-0.420
Midheight Rib Drift 12	536	18.90	1.83	-0.926	-0.228
	829	18.90	3.05	-0.326	-2.012
	905	18.29	3.66	0.366	-5.408
	933	28.802	10.56	-0.007	-0.854
Centerline Roof Drift 12	962	17.07	3.66	0.191	-7.000
Centerline Floor Demo Drift	971	25.00	12.19	-0.097	-1.147
Midheight Rib Demo Drift	984	21.95	14.02	-0.145	-1.401
Midheight Rib Demo Drift	999	28.04	14.02	-0.118	-0.951
Centerline Roof Demo Drift	1198	25.00	15.85	-0.177	-1.166
	1355	22.37	26.43	-0.296	-1.248
	1425	25.00	28.10	-0.281	-1.125

Table A.2

DISPLACEMENTS AFTER EXCAVATION OF DEMO DRIFT (T=3)

Location	Node	x m	y m	Ux mm	Uy mm
Centerline Floor-Drift 12	223	17.07	0.0	0.160	7.259
	232	25.00	0.0	0.247	0.055
	494	20.60	4.48	0.622	-0.912
Midheight Rib-Drift 12	524	15.24	1.83	1.448	-1.024
Midheight Rib-Drift 12	536	18.90	1.83	-0.404	0.113
	829	18.90	3.05	0.425	-1.765
	905	18.29	3.66	1.265	-5.639
	933	28.802	10.56	0.128	-0.304
Centerline Roof-Drift 12	962	17.07	3.66	0.976	-7.582
Centerline Floor-Demo Drift	971	25.00	12.19	-0.054	1.956
Midheight Rib-Demo Drift	984	21.95	14.02	-0.233	-2.520
Midheight Rib-Demo Drift	999	28.04	14.02	0.335	-1.585
Centerline Roof-Demo Drift	1198	25.00	15.85	0.115	-5.560
	1355	22.37	26.43	-0.067	-3.394
	1425	25.00	28.10	-0.240	-3.108

APPENDIX B

This report simulates the behavior of underground openings in G-tunnel; therefore, this report contains no data from, or for inclusion in, the RIB and/or SEPDB.

DISTRIBUTION LIST

1 J. W. Bartlett, Director (RW-1)
Office of Civilian Radioactive
Waste Management
U.S. Department of Energy
1000 Independence Avenue, S.W.
Washington, D.C. 20585

1 F. G. Peters, Deputy Director (RW-2)
Office of Civilian Radioactive
Waste Management
U.S. Department of Energy
1000 Independence Avenue, S.W.
Washington, D.C. 20585

1 T. H. Isaacs (RW-4)
Office of Strategic Planning
and International Programs
Office of Civilian Radioactive
Waste Management
U.S. Department of Energy
1000 Independence Avenue, S.W.
Washington, D.C. 20585

1 J. D. Saltzman (RW-5)
Office of External Relations
Office of Civilian Radioactive
Waste Management
U.S. Department of Energy
1000 Independence Avenue, S.W.
Washington, D.C. 20585

1 Samuel Rousso (RW-10)
Office of Program and Resources
Management
Office of Civilian Radioactive
Waste Management
U.S. Department of Energy
1000 Independence Avenue, S.W.
Washington, D.C. 20585

1 J. C. Bresee (RW-10)
Office of Civilian Radioactive
Waste Management
U.S. Department of Energy
1000 Independence Avenue, S.W.
Washington, D.C. 20585

1 C. P. Gertz (RW-20)
Office of Geologic Disposal
Office of Civilian Radioactive
Waste Management
U.S. Department of Energy
1000 Independence Avenue, S.W.
Washington, D.C. 20585

1 S. J. Brocoum (RW-22)
Analysis and Verification Division
Office of Civilian Radioactive
Waste Management
U.S. Department of Energy
1000 Independence Avenue, S.W.
Washington, D.C. 20585

1 D. D. Shelor (RW-30)
Office of Systems and Compliance
Office of Civilian Radioactive
Waste Management
U.S. Department of Energy
1000 Independence Avenue, S.W.
Washington, D.C. 20585

1 J. Roberts (RW-33)
Office of Civilian Radioactive
Waste Management
U.S. Department of Energy
1000 Independence Avenue, S.W.
Washington, D.C. 20585

1 G. J. Parker (RW-332)
Office of Civilian Radioactive
Waste Management
U.S. Department of Energy
1000 Independence Avenue, S.W.
Washington, D.C. 20585

1 Associate Director (RW-40)
Office of Storage and Transportation
Office of Civilian Radioactive
Waste Management
U.S. Department of Energy
1000 Independence Avenue, S.W.
Washington, D.C. 20585

1 Associate Director (RW-50)
Office of Contract Business
Management
Office of Civilian Radioactive
Waste Management
U.S. Department of Energy
1000 Independence Avenue, S.W.
Washington, D.C. 20585

1 C. G. Russomanno (RW-52)
Office of Civilian Radioactive
Waste Management
U.S. Department of Energy
1000 Independence Avenue, S.W.
Washington, D.C. 20585

1 D. U. Deere, Chairman
Nuclear Waste Technical
Review Board
1100 Wilson Blvd. #910
Arlington, VA 22209-2297

1 Dr. Clarence R. Allen
Nuclear Waste Technical Review Board
1000 E. California Blvd.
Pasadena, CA 91106

1 Dr. John E. Cantlon
Nuclear Waste Technical Review Board
1795 Bramble Dr.
East Lansing, MI 48823

1 Dr. Melvin W. Carter
Nuclear Waste Technical Review Board
4621 Ellisbury Dr., N.E.
Atlanta, GA 30332

1 Dr. Donald Langmuir
Nuclear Waste Technical Review Board
109 So. Lookout Mountain Cr.
Golden, CO 80401

1 Dr. D. Warner North
Nuclear Waste Technical Review Board
Decision Focus, Inc.
4984 El Camino Real
Los Altos, CA 94062

1 Dr. Dennis L. Price
Nuclear Wast Technical Review Board
1011 Evergreen Way
Blacksburg, VA 24060

1 Dr. Ellis D. Verink
Nuclear Waste Technical Review Board
4401 N.W. 18th Place
Gainesville, FL 32605

5 C. P. Gertz, Project Manager
Yucca Mountain Project Office
U.S. Department of Energy
P.O. Box 98608--MS 523
Las Vegas, NV 89193-8608

1 C. L. West, Director
Office of External Affairs
DOE Field Office, Nevada
U.S. Department of Energy
P.O. Box 98518
Las Vegas, NV 89193-8518

12 Technical Information Officer
DOE Field Office, Nevada
U.S. Department of Energy
P.O. Box 98518
Las Vegas, NV 89193-8518

1 P. K. Fitzsimmons, Director
Health Physics & Environmental
Division
DOE Field Office, Nevada
U.S. Department of Energy
P.O. Box 98518
Las Vegas, NV 89193-8518

1 D. R. Elle, Director
Environmental Protection Division
DOE Field Office, Nevada
U.S. Department of Energy
P.O. Box 98518
Las Vegas, NV 89193-8518

1 Repository Licensing & Quality
Assurance Project Directorate
Division of Waste Management
U.S. Nuclear Regulatory Commission
Washington, D.C. 20555

1 Senior Project Manager for Yucca
Mountain Repository Project Branch
Division of Waste Management
U.S. Nuclear Regulatory Commission
Washington, D.C. 20555

1 NRC Document Control Desk
Division of Waste Management
U.S. Nuclear Regulatory Commission
Washington, D.C. 20555

1 P. T. Prestholt
NRC Site Representative
301 E. Stewart Ave.
Las Vegas, NV 89101

1 E. P. Binnall
Field Systems Group Leader
Building 50B/4235
Lawrence Berkeley Laboratory
Berkeley, CA 94720

1 Center for Nuclear Waste
Regulatory Analyses
6220 Culebra Road
Drawer 28510
San Antonio, TX 78284

3 L. J. Jardine
Technical Project Officer for YMP
Mail Stop L-204
Lawrence Livermore National Laboratory
P.O. Box 808
Livermore, CA 94550

4 R. J. Herbst
Technical Project Officer for YMP
N-5, Mail Stop J521
Los Alamos National Laboratory
P.O. Box 1663
Los Alamos, NM 87545

1 H. N. Kalia
Exploratory Shaft Test Manager
Los Alamos National Laboratory
Mail Stop 527
101 Convention Center Drive
Suite 820
Las Vegas, NV 89109

1 J. F. Divine
Assistant Director for Engineering Geology
U.S. Geological Survey
106 National Center
12201 Sunrise Valley Drive
Reston, VA 22092

6 L. R. Hayes
Technical Project Officer
Yucca Mountain Project Branch--MS 425
U.S. Geological Survey
P.O. Box 25046
Denver, CO 80225

1 V. R. Schneider
Asst. Chief Hydrologist--MS 414
Office of Program Coordination & Technical Support
U.S. Geological Survey
12201 Sunrise Valley Drive
Reston, VA 22092

1 R. B. Raup, Jr.
Geological Division Coordinator
MS 913
Yucca Mountain Project
U.S. Geological Survey
P.O. Box 25046
Denver, CO 80225

1 D. H. Appel, Chief
Hydrologic Investigations Program
MS 421
U.S. Geological Survey
P.O. Box 25046
Denver, CO 80225

1 E. J. Helley
Branch of Western Regional Geology
MS 427
U.S. Geological Survey
345 Middlefield Road
Menlo Park, CA 94025

1 Chief
Nevada Operations Office
U.S. Geological Survey
101 Convention Center Drive
Suite 860, MS 509
Las Vegas, NV 89109

1 D. Zesiger
U.S. Geological Survey
101 Convention Center Dr.
Suite 860 - MS509
Las Vegas, NV 89109

1 R. V. Watkins, Chief
Project Planning and Management
U.S. Geological Survey
P.O. Box 25046
421 Federal Center
Denver, CO 80225

1 A. L. Flint
U.S. Geological Survey
MS 721
P.O. Box 327
Mercury, NV 89023

1 D. A. Beck
U.S. Geological Survey
1600 E. Tropicana, Suite 115
Las Vegas, NV 89132

1 P. A. Glancy
U.S. Geological Survey
Federal Building, Room 224
Carson City, NV 89701

1 Sherman S. C. Wu
Branch of Astrogeology
U.S. Geological Survey
2255 N. Gemini Drive
Flagstaff, AZ 86001

1 J. H. Sass
Branch of Tectonophysics
U.S. Geological Survey
2255 N. Gemini Drive
Flagstaff, AZ 86001

1 DeWayne A. Campbell
Technical Project Officer for YMP
Bureau of Reclamation
Code D-3790
P.O. Box 25007
Denver, CO 80225

1 S. M. Dash
Science Applications International Corp.
14062 Denver West Parkway, Suite 255
Golden, CO 80401

1 K. W. Causseaux
NHP Reports Chief
U.S. Geological Survey
421 Federal Center
P.O. Box 25046
Denver, CO 80225

1 V. M. Glanzman
U.S. Geological Survey
913 Federal Center
P.O. Box 25046
Denver, CO 80225

1 J. H. Nelson
Technical Project Officer for YMP
Science Applications International Corp.
101 Convention Center Drive
Suite 407
Las Vegas, NV 89109

2 SAIC-T&MSS Library
Science Applications International Corp.
101 Convention Center Drive
Suite 407
Las Vegas, NV 89109

1 Elaine Ezra
YMP GIS Project Manager
EG&G Energy Measurements, Inc.
Mail Stop D-12
P.O. Box 1912
Las Vegas, NV 89125

1 R. E. Jackson, Program Manager
Roy F. Weston, Inc.
955 L'Enfant Plaza, Southwest
Washington, D.C. 20024

1 Technical Information Center
Roy F. Weston, Inc.
955 L'Enfant Plaza, Southwest
Washington, D.C. 20024

1 D. Hedges, Vice President,
Quality Assurance
Roy F. Weston, Inc.
4425 Spring Mountain Road, Suite 300
Las Vegas, NV 89102

1 D. L. Fraser, General Manager
Reynolds Electrical & Engineering Co.
Mail Stop 555
P.O. Box 98521
Las Vegas, NV 89193-8521

1 R. F. Pritchett
Technical Project Officer for YMP
Reynolds Electrical & Engineering Co.
MS 408
P.O. Box 98521
Las Vegas, NV 89193-8521

1 B. W. Colston
General Manager & President
Las Vegas Branch
Raytheon Services Nevada
Mail Stop 416
P.O. Box 95487
Las Vegas, NV 89193-5487

1 R. L. Bullock
Technical Project Officer for YMP
Raytheon Services Nevada
Suite P250, MS 403
101 Convention Center Drive
Las Vegas, NV 89109

1 R. E. Lowder
Technical Project Officer for YMP
MAC Technical Services
101 Convention Center Drive
Suite 1100
Las Vegas, NV 89109

1 C. K. Hastings, Manager
PASS Program
Pacific Northwest Laboratories
P.O. Box 999
Richland, WA 99352

1 A. T. Tamura
Science and Technology Division
Office of Scientific and Technical Information
U.S. Department of Energy
P.O. Box 62
Oak Ridge, TN 37831

1 Carlos G. Bell, Jr.
Professor of Civil Engineering
Civil and Mechanical Engineering Department
University of Nevada, Las Vegas
4505 South Maryland Parkway
Las Vegas, NV 89154

1 C. F. Costa, Director
Nuclear Radiation Assessment Division
U.S. Environmental Protection Agency
Environmental Monitoring Systems Laboratory
P.O. Box 93478
Las Vegas, NV 89193-3478

1 ONWI Library
Battelle Columbus Laboratory
Office of Nuclear Waste Isolation
505 King Avenue
Columbus, OH 43201

1 T. Hay, Executive Assistant
Office of the Governor
State of Nevada
Capitol Complex
Carson City, NV 89710

3 R. R. Loux, Jr.
Executive Director
Nuclear Waste Project Office
State of Nevada
Evergreen Center, Suite 252
1802 North Carson Street
Carson City, NV 89710

1 C. H. Johnson
Technical Program Manager
Nuclear Waste Project Office
State of Nevada
Evergreen Center, Suite 252
1802 North Carson Street
Carson City, NV 89710

1 John Fordham
Water Resources Center
Desert Research Institute
P.O. Box 60220
Reno, NV 89506

1 Dr. Martin Mifflin
Water Resources Center
Desert Research Institute
2505 Chandler Avenue
Suite 1
Las Vegas, NV 89120

1 Eric Anderson
Mountain West Research-Southwest Inc.
2901 N. Central Avenue #1000
Phoenix, AZ 85012-2730

1 Department of Comprehensive Planning
Clark County
225 Bridger Avenue, 7th Floor
Las Vegas, NV 89155

1 Planning Department
Nye County
P.O. Box 153
Tonopah, NV 89049

1 Lincoln County Commission
Lincoln County
P.O. Box 90
Pioche, NV 89043

5 Judy Foremaster
City of Caliente
P.O. Box 158
Caliente, NV 89008

1 Economic Development Department
City of Las Vegas
400 East Stewart Avenue
Las Vegas, NV 89101

1 Community Planning & Development
City of North Las Vegas
P.O. Box 4086
North Las Vegas, NV 89030

1 Director of Community Planning
City of Boulder City
P.O. Box 367
Boulder City, NV 89005

1 Commission of the European
Communities
200 Rue de la Loi
B-1049 Brussels
BELGIUM

2 M. J. Dorsey, Librarian
YMP Research and Study Center
Reynolds Electrical & Engineering
Co., Inc.
MS 407
P.O. Box 98521
Las Vegas, NV 89193-8521

1 Amy Anderson
Argonne National Laboratory
Building 362
9700 So. Cass Avenue
Argonne, IL 60439

1 1425 J. H. Biffle
1 1510 J. C. Cummings
5 1514 R. L. Johnson
1 1514 H. S. Morgan
1 1540 J. R. Assay
1 1544 J. R. Assay, Actng.
1 1545 D. R. Martinez
1 1550 C. W. Peterson
1 6300 T. O. Hunter
1 6310 T. E. Blejwas, Actg.
1 6310A L. E. Shephard
1 6311 A. L. Stevens
1 6312 F. W. Bingham
1 6313 L. S. Costin
2 6313 S. J. Bauer
1 6315 F. B. Nimick, Actg.
1 6316 R. P. Sandoval
1 6317 S. Sinnock
2 6318 R. J. Macer for
100/124212/SAND88-0810/QA
2 6318 L. J. Erickson for DRMS
file 55/F08-11/1/89
1 6319 R. R. Richards
5 3141 S. A. Landenberger
8 3145 Document Processing
for DOE/OSTI
3 3151 G. C. Claycomb
20 6341 WMT Library
1 6410 D. J. McCloskey, Actg.
1 8523-2 Central Technical Files

END

DATE FILMED

01/02/92